AMERICAN UNIVERSITY OF BEIRUT

Mechanistic DFT Studies on the Protonation of Transition Metal-Nitride Complexes and the Decomposition of Metal-Alkoxides

by
Mohamad A. Ataya

A thesis
submitted in partial fulfillment of the requirements
for the degree of Master of Science
to the Department of Chemistry
of the Faculty of Arts and Sciences
at the American University of Beirut

Beirut, Lebanon
June 2020

AMERICAN UNIVERSITY OF BEIRUT

Mechanistic DFT Studies on the Protonation of Transition Metal-Nitride Complexes and the Decomposition of Metal-Alkoxides

by

Mohamad A. Ataya

Approved by:

_____

Dr. Faraj Hasanayn, Professor   Advisor

Chemistry

_____

Dr. Kamal Bouhadir, Professor   Member of Committee

Chemistry

_____

Dr. Houssam El-Rassy, Associate Professor   Member of Committee

Chemistry

Date of thesis defense: June 12, 2020

AMERICAN UNIVERSITY OF BEIRUT

THESIS, DISSERTATION, PROJECT
RELEASE FORM

Student Name: _____
Last   First   Middle

◯ Master's Thesis   ◯ Master's Project   ◯ Doctoral Dissertation

☐   I authorize the American University of Beirut to: (a) reproduce hard or electronic copies of my thesis, dissertation, or project; (b) include such copies in the archives and digital repositories of the University; and (c) make freely available such copies to third parties for research or educational purposes.

☐   I authorize the American University of Beirut, to: (a) reproduce hard or electronic copies of it; (b) include such copies in the archives and digital repositories of the University; and (c) make freely available such copies to third parties for research or educational purposes after: **One ___ year from the date of submission of my thesis, dissertation or project.**
Two ___ years from the date of submission of my thesis , dissertation or project.
Three ___ years from the date of submission of my thesis , dissertation or project.

_____
Signature   Date

This form is signed when submitting the thesis, dissertation, or project to the University Libraries

Acknowledgements

An Abstract of the Thesis of

Mohamad Ataya   for   Master of Science
                         Major: Chemistry

Title: Mechanistic DFT Studies on the Protonation of Transition Metal-Nitride Complexes and the Decomposition of Metal-Alkoxides

Knowledge of reaction mechanisms is of fundamental interest in chemistry. Understanding mechanisms can have immediate practical implications in the optimization of known reactions and the discovery of new ones. The advents in computer hardware and software technologies makes it possible at present to investigate reaction mechanisms of chemically relevant systems using modern quantum chemical methods such as density functional theory (DFT). In this thesis we report results on two mechanistic DFT investigations. The first investigation pertains to a peculiar observed reaction between four coordinate pincer-ligated metal-nitride complexes and carboxylic acid derivatives. The reaction converts the metal-nitride bond into a metal-ammine bond by an intramolecular metal-ligand cooperative (MLC) proton coupled electron transfer mode. The resulting ammine complex has an octahedral geometry with the benzoate anion acting as a chelating ligand. We calculate a series of elementary steps leading to the given transformation and we study how the activation and reaction energies change as a function of the carboxylic acid derivative and the metal center. Surprisingly, we find nearly no effects of the acid on the rates of the first step of metal-nitride protonation. Analysis of the results using thermodynamic cycles show this behavior follows because nitride protonation in this system in fact proceeds by a concerted bifunctional addition step in which the proton from the carboxylic acid goes to the nitride while the carbonyl group of the acid simultaneously coordinates to the metal. The stronger acids that favor nitride protonation appear to simply disfavor coordination of the carbonyl to the metal. The two effects thus cancel out. The calculations reveal more pronounced dependence of the reaction rates on the nature of the metal. In all cases, the calculations reveal that the carboxylic acid addition step is not the rate limiting step. In light of this observation we explored the possibility of coupling the carboxylic acid addition step with an external hydrogen atom donor. The calculations predict a mixture of carboxylic acid and

TEMPOH is likely to transform the metal-nitride bond to metal-ammine one at rates comparable to the intramolecular ones involving the ligand. Our second investigation pertains to the mechanism and products of decomposition of the octahedral complex trans-(H)(OMe)Ir(Ph)(PMe$_3$)$_3$. In the presence of methanol as a catalyst, this complex is known to decompose into the trans-dihydride complex trans-(H)$_2$Ir(Ph)(PMe$_3$)$_3$ along with organic products that were reported as formaldehyde oligomers. Our detailed calculations on this system reproduce the experimental observation that methanol can catalyze decomposition by an unconventional outer-sphere beta-hydride elimination from the metal-alkoxide to give the observed trans-dihydride and formaldehyde. However, our calculations indicate strongly that this step is thermodynamically uphill. As an alternative to formaldehyde oligomerization, we show a formaldehyde molecule produced from one metal-alkoxide can react with another metal-alkoxide to give another trans-dihydride complex and methyl formate. The latter reaction is computed to be highly exergonic and can be viewed as an H/OMe metathesis taking place by an outer-sphere mechanism. The calculations also show that a methyl formate product can in turn undergo another low barrier H/OMe metathesis with another metal alkoxide to give dimethyl carbonate.

Contents

List of Figures

Chapter 1

Computational Methods

1.1   Introduction

According to the 20th century English physicist Paul Dirac, "The underlying physical laws necessary for the mathematical theory of a large part of physics and the whole of chemistry are thus known, and the difficulty is only that the exact application of these laws leads to equations much too complicated to be soluble" [1]. Towards the solubility of such complex mathematics, the field of computational chemistry has been designed and developed to simulate chemical structures and reactions numerically, based in full or in part on the fundamental laws of physics. Briefly, computational chemistry can be used to compute, but not limited to, geometries (bond lengths, angles and torsion angles), energies (heat of formation, activation energy), electronic properties (moments, charges electron affinity) spectroscopic properties (vibrational modes, chemical shift) and bulk properties (volumes, surface areas viscosity). Furthermore, it can be used to study interactions between molecules (host-guest chemistry, drug design), develop and elucidate reaction mechanisms and give insight into protein folding problems and bioinformatics. Across the literature, we observe the supporting role of computational chemistry by complementing and explaining experimental results. Even more, a chemist employing the computational tools can go where experimental difficulty and limits can be a barrier such as studying transition states and intermediates.

From an environmental perspective, computational chemistry is in essence an absolute green method to acquire chemical knowledge given the new developments of green alternatives to energy. For example, using density functional theory (DFT) allows for the study of a reaction pathway, including its intermediates, transition states from which kinetic and thermodynamic information can be extracted. Numerous examples in the chemical literature employ this method to study catalytic and other systems (including the work in this thesis) involving

metals such as molybdenum [2], rhodium [3] and ruthenium [4]. The reduction in use and disposal of catalysts, reagents and organic solvents has a great impact environmentally and in exercising the principles of a green chemistry approach.

Given, the current world events, namely the COVID-19 pandemic, we now see the emergence of computational chemistry as a leading method of discovery. Running experimental procedures and studying the effectiveness of a drug can take time, which in turn can have unexpected social and economic outcomes. According to PHARMA, a leading RD pharmaceutical research firm, for a drug to be developed, tested and marketed it could take at least 10 years along with an estimated cost of $2.6 billion. The employment of computational chemistry can shorten the time required to locate a lead molecule with therapeutic properties and decrease the time used in running bench work and human errors. The in silico studies performed where able to elucidate the structure of the novel coronavirus, and predict possible inhibition mechanism and drugs. In one study, the researchers were able to identify a single protein marker and perform drug binding tests successful in activating an inhibiting mechanism [5].

1.2 Methods of Analysis and Inquiry in Present Study

The purpose of this thesis is for purely theoretical studies. All calculations will be carried out on the IBM High Performance Computer available at AUB, which has the quantum chemical software Gaussian 09 [6]. Following previous studies, geometry minimization will be done using some of the more popular density functional theory (DFT) levels such as the M06 [7], M06L [8] and wB97XD [9] levels. The transition metals will carry relativistic effective core potentials (ECP) [10], which is a standard methodology in computational chemistry. Those potentials are used to replace the inner core electrons of atoms or molecules by an effective potential and only the valence electrons are used in the calculations. The basis set will be of at least a 6-311G(d,p) quality for the first project and Def2TZVP basis set for the second project. Solvent effects will be included using some of the modern continuum methodologies. In some cases, the effects of explicit solvent molecules on the activation and reactions energies will be examined. All minima and transition states will be characterized using normal mode vibrational analyses. Free energies will be determined using statistical mechanics methods at standard state conditions (1 atm, and 298 K). Natural bonding orbital analysis was conducted using the NBO program present in the Gaussian suite [11]. The visualization of NBO topology was done using Chemcraft [12] The visualization of the computed complexes was carried out on the Gaussview software [13]. The

quantum theory of atoms in molecules (QTAIM) is the method chosen to compute the atomic charges of the complexes given its accuracy and reliability in comparison to experimental data. The QTAIM computations were conducted using the AIMALL software suite [14].

Chapter 2

DFT Study of a New Bifunctional Reaction Between Carboxylic Acid Derivatives and a Ruthenium Nitride Complex

2.1 Introduction

Ammonia is among the most commonly consumed chemicals in the world with an estimated demand of around 160 million tonnes annually, which is also expected to increase [15]. The data shows an increasing trend suggesting a growing demand worldwide for ammonia. The increased demand for ammonia production lies in prominent historical events. In the late 1800's, impacted by the industrial revolution, the human population began to increase in an unprecedented way, consequently causing a rising demand in agricultural products such as grains. To meet the new demand, farmers began exploring ways to increase the amount of nitrogen in the soil thus making new areas more crop productive. At the time, they mixed animal manure as a method of adding nitrates into the soil. However, faced with a high degree of human population growth, science and specifically chemistry became involved in the production of fixed nitrogen, as was observed in natural systems. As Sir William Crookes declared famously in 1898, with regards to the need of more fixed nitrogen, "*it is the chemist who must come to rescue*"[16].

2.2 The Haber-Bosch Process

The rescue came in by Fritz Haber (1868 - 1934), on July 2 1909. Haber and a colleague in the laboratory at Karlsruhe produced a continuous flow of liquid ammonia, about 473 mL in five hours, from its elements hydrogen and nitrogen

fed into a hot 12.7 cm wide iron tube that was 61 cm tall, the gases at 200 atm over an osmium metal catalyst[16]. This achievement provided the proof of concept, which now required a scaling up process in order to meet the global demand. The process was industrialized by the notable contribution of Carl Bosch, who led the synthesis into a world scale. Next came the construction of the first plant which began in 1912 Oppau, and was finished in 1914, producing 20 tons of ammonia daily, by utilizing a cheap iron-based catalyst. The remarkable work of Haber was awarded the 1918 noble prize in chemistry. The Haber-Bosch chemical reaction is shown in Figure 2.1.

$$N_{2(g)} + 3H_{2(g)} \xrightarrow[\substack{T = 400\text{ - }600\ ^oC \\ P = 200\text{ - }300\ atm}]{Catalyst} 2NH_{3(g)}$$
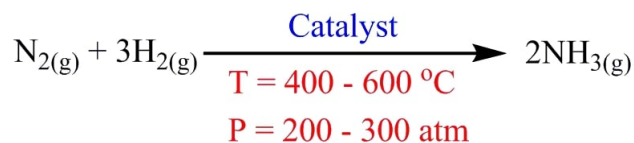
Figure 2.1: The Haber-Bosch process for the synthesis of ammonia from its elements.

While the goal of the chemist was realised, it did not come without a heavy price. The impact of the process was not only on the population size, but also on the use of fossil fuel. The Haber-Bosch process is an energy expensive alternative. It requires 400 - 600°C as temperature and 200 - 300 atm as pressure, which are all provided by burning fossil fuel. In fact, the synthesis of ammonia uses up to 5% of the world's natural gas production [17], equivalent to 1-2% of the world's annual energy consumption[18]. Given these facts, along with science taking a critical turn for green and environmental friendly approach, there is now great interest to develop alternative routes to ammonia that may be more energy efficient than the process.

2.3 Alternative Methods to Ammonia Synthesis

2.3.1 Molybdenum Complexes: Cleavage of Dinitrogen

In 1995, Cummins and Laplaza reported the cleavage of N_2 by a three-coordinate molybdenum(III) complex [19]. They attempted to utilize the relatively inert and strongly bonded N_2 molecule by cleaving it into two metal-nitrido complexes. They reported the reductive cleavage of N_2 using a molybdenum complex. The process is illustrated in Figure 2.2.

The starting material has a red-orange color, which when the group attempted to purify (ethyl ether, 0.1 M, -35°C) by re-crystallization under N_2 atmosphere, it turned into a purple colored solution. The color change was accompanied by a change in the ^{1}H NMR spectra; a 64 ppm signal was replaced by a single peak at
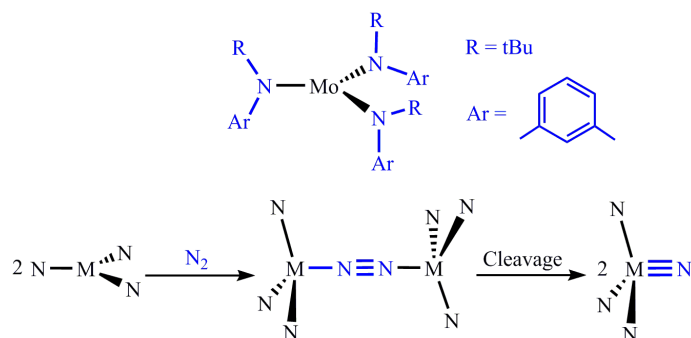
Figure 2.2: The reductive cleavage of N_2 using a molybdenum complex.

14 ppm. The purple solution was warmed to 30°C, in order to remove the volatile material, which led to the change in the color of the solution into gold (then amber) and loss of its para-magnetic properties. ^{1}H NMR analysis revealed that the final complex was a Mo(IV) bonded to a terminal nitride. This conclusion was based on comparing the spectra of this study with that of a previous study done by the same group. At the time, four coordinate molybdenum nitrido complexes were known, and the driving force for the cleavage of the N_2 was attributed to the thermodynamic preference for the formation of the nitride strong bond.

In heterogeneous catalysis the cleavage of N_2 has been confirmed to be the first step in the Haber-Bosch process [20]. This is then followed by step-wise hydrogenation to form ammonia. An analogous homogeneous catalytic process has been envisioned using the same elementary steps; splitting of N_2 forming two metal nitride complexes followed by hydrogenolysis to make ammonia. While the work of Cummins demonstrated the viability of cleaving the N_2 bond making two metal nitrido complexes, the hydrogenation of the product has been a major obstacle due to the stability of the nitride bond.

Building on the use of pincer chelated complexes, in 2012 Schrock and coworkers reported the cleavage of dinitrogen using a molybdenum(IV) nitride complex [21]. First, they demonstrated the cleavage of N_2 giving a nitrido complex (Figure 2.3).
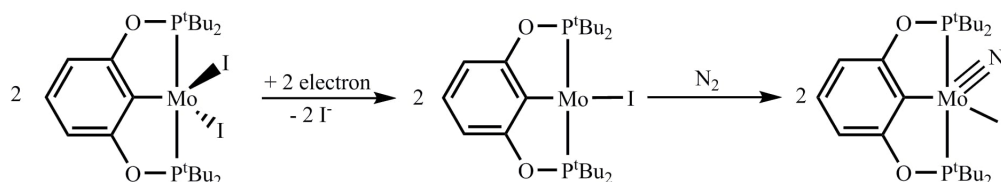
Figure 2.3: The cleavage of N_2 using a $(tBuPOCOP)MoI_2$ complex.

The next step was to form ammonia by protonation of the nitride, envisioned by the group as an electro-catalytic cycle of simple design (Figure 2.4).
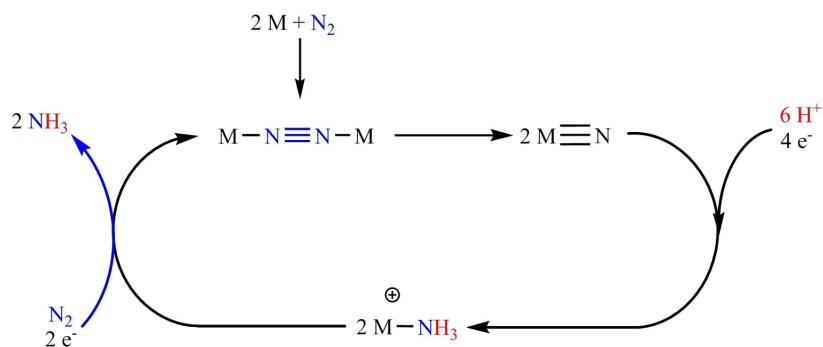
Figure 2.4: Simplified design for an electro-cataytic cycle for ammonia synthesis.

The protonation of the nitrido complex was performed using $[Et_3NH][BAr'4]$ in benzene giving a yellow solid. A series of NMR experiments were performed in order to elucidate the structure of the yellow solid. The results of the NMR study showed that there were nonequivalent phosphorus nuclei. Further NMR studies led to the proposition that the protonation occurred across the metal phosphine bond as shown in Figure 2.5.
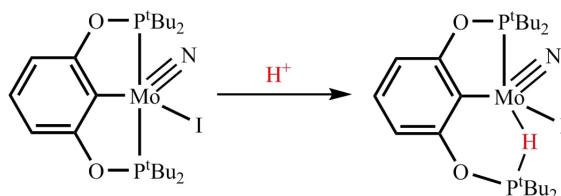
Figure 2.5: The protonation of the nitride complex led to an unexpected result.

2.4   Background and Plan for the Present Study

Schneider and coworkers synthesized and isolated a rare example of four-coordinate ruthenium(IV) nitride complex using the anionic PNP pincer ligand where N is an anionic amido center (**1**, Figure 2.6). This complex has three sites that can in principle be protonated by an acid, namely: the nitride nitrogen, the metal center and the amido nitrogen of the PNP ligand. Experimentally, reaction between **1** and the lutidinium ion leads to selective quantitative protonation at the amido nitrogen. The resulting cationic complex **2** could be isolated, and it was characterized by single X-ray analysis [22]. Treatment of the cationic complex **1** with excess acid [HLut][BF$_4$] does not result in any further protonation.
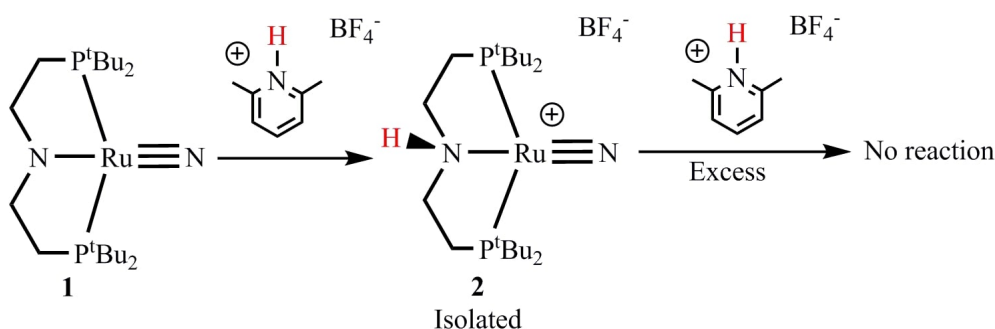
Figure 2.6: The selective protonation of the pincer amide on **1** using [$HLut$][BF_4].

During the course of an electrochemical study of the complex **2**, Miller and coworkers discovered that treatment of **2** with one equivalent 4-Methoxybenzoic acid in THF results in a most peculiar and unusual reaction described in Figure 2.7.
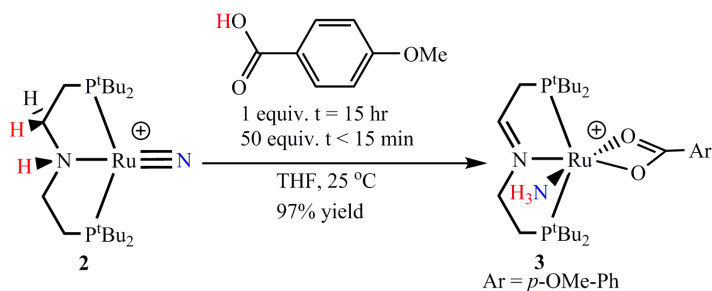
Figure 2.7: The formation of a metal ammine product by the new reaction between 4-methoxybenzoic acid and **2**.

The transformation in Figure 2.7 is a complex transformation that has many components. First, the ruthenium nitride bond is transformed into a ruthenium ammine bond. This specific transformation is formally a three proton – two electron process (3H+/2e-) in which the oxidation state of the metal center is changed

from Ru(IV) to Ru(II). The three protons involved in this reaction come from different parts. The carboxylic acid derivative obviously provides one proton. Two other protons are provided from the pincer PNP, one from the amine center and one from the adjoining carbon center. The two electrons both come from the ligand, leading to the formation of an imine C=N bond. The transformation is accompanied with κ2-coordination of the benzoate anion to provide a final octahedral coordination sphere around the metal. The final cationic octahedral Ru-ammine product **3** is formally an 18-electron complex that has a d6-Ru(II) metal center and formally satisfies the 18-electron rule.

In collaboration with Miller, our group had previously proposed a plausible mechanism for the given reaction and supported it with preliminary DFT calculations. The proposed mechanism is outlined in Figure 2.8.
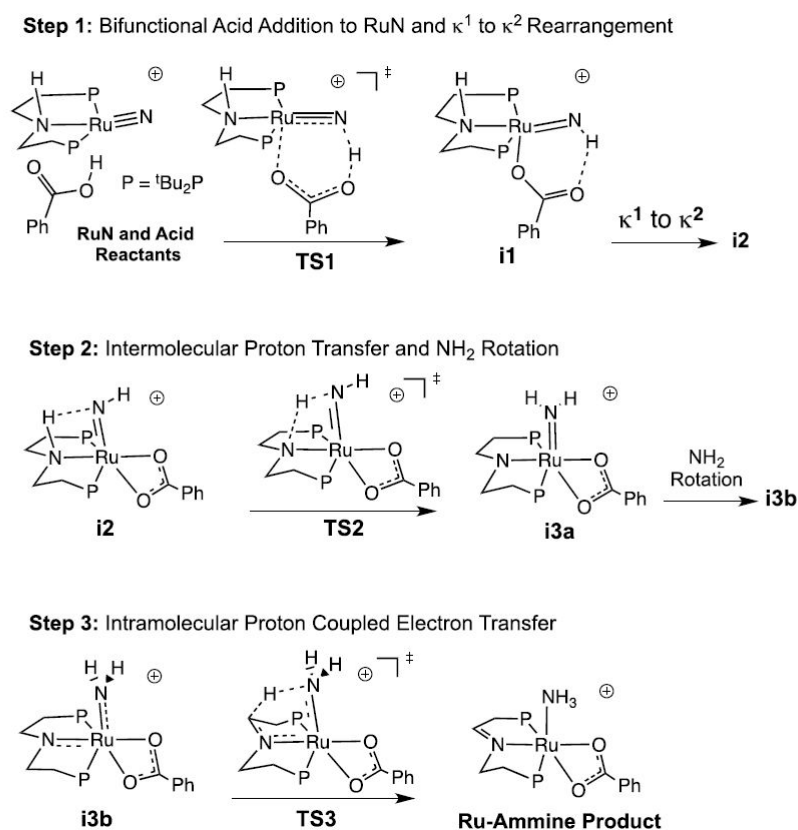
Figure 2.8: Proposed mechanism for Ru-ammine formation from Ru-nitride and benzoic acid.

The proposed mechanism has three major steps. The entry step is an unconventional bifunctional reaction mode in which the proton from the OH group of the acid is transferred to the nitride ligand while the carbonyl group of the acid coordinates to the metal. Bifunctional means two reactions centers are involved

in the step the metal and the nitride ligand. Intermediate **i1** has the one of the benzoate oxygen atoms coordinated to the metal in $\kappa 1$-mode and has the hydrogen bond between the newly formed N-H bond and the second oxygen of the benzoate. The formation of **i1** was reported to proceed through a pericyclic transition state **TS1**. The calculations identified another octahedral form of intermediate **i1** in which the protonated nitride group is now cis to the central amine of the PNP ligand and the benzoate coordination mode has changed from $\kappa 1$ to $\kappa 2$-coordination. This intermediate is labeled **i2** in Figure 2.8.

Intermediate **i2** places the amino pincer proton next to the nitrogen of the imido NH ligand. The second step proposed in Figure 2.8 is a proton transfer step from the amine to the imide taking place through **TS2** to give **i3a**. **i3a** is formally a di-amide octahedral complex. The calculations identified a rotamer of **i3a** that orients the plane of the $RuNH_2$ group toward the C-H bond in the backbone. This rotamer is labelled **i3b** in the figure.

Finally, the last step in Figure 2.8 involves the formation of the Ru-ammine complex from **i3b**. This is a complex step that does three things at the same time. First a proton is lost from one of the carbons in the backbone of the PNP ligand. As the proton leaves the carbon center, the lone pair that is being produced on the carbon center moves to the central carbon of the PNP ligand to make a C=N double bond. This movement of the electrons from carbon to nitrogen is accompanied with further movement of another pair of electrons from nitorgen of the PNP ligand to the metal. The net reaction in step 3 in the figure is therefore a Proton Coupled Electron Transfer (PCET) when a proton moves to the carbon center to the nitrogen and 2 electrons move concomitantly from the ligand nitrogen to the metal. It is this step that changes the oxidation state from of the metal from Ru(IV) to Ru(II).

The transformation in Figure 2.7 has no precedence. Likewise, the proposed reaction mechanism has no prior similarities. Many aspects of the proposed elementary reactions in this mechanism are still not well understood. In first part of the given thesis we extend the use to of DFT calculations to gain a deeper understanding of the elementary steps and to explore their scope. We can divide the study into three parts:

Part 1: We begin our study by addressing the nature of bonding in the RuN bond of the reactant cationic complex. This investigation is done in an attempt to understand why the given bond is kinetically inert to protonation by conventional acids. For this purpose we have undertaken detailed electronic structure analyses using two charge partitioning schemes: **(i)** the Natural Bonding Orbitals (NBO) scheme developed by Weinhold [23], and **(ii)** the Quantum Theory of Atoms in Molecules (QTAIM) scheme developed by Bader [14]. We attempt

to gain insight into the changes in the electronic structure of the selected bond across the reaction pathway.

Part 2: In the second part of this investigation we conduct a detailed structure-activity study of the given RuN to Ru-NH$_3$ transformation. In this part we determine the effects of the acid and the metal on the reaction rates and energies of the transformation.

Part 3: In the last part of our study on the given reaction we try to use what we learned in the second part (the structure-activity study) to identify new reactions. The reaction reported before uses carboxylic acid derivatives to induce intramolecular PCET. We use the calculations to explore if carboxylic acid can induce other reactions, such as intermolecular hydrogen atom transfer.

2.5 NBO and QTAIM Analysis

An important objective of the present theoretical work is to use theory to monitor the electronic structure changes during the course of the reaction. To this end we rely on two computational method. The first is the natural bonding orbital analysis (NBO) which allows for the visualization and the study of the composition of the orbital interactions between bonding atoms. The second method computes the atomic charges using QTAIM, which relies on the inherent electronic density of a given system to compute atomic properties.

2.5.1 NBO Analysis
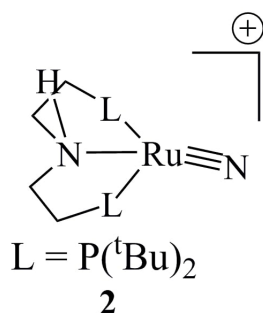
Figure 2.9: The pincer chelated ruthenium complex involved in the bifunctional reaction.

We begin by taking a look at the structure of **2**, which is classified as a ruthenium nitride complex, with a protonated pincer. The short Ru-N bond (1.6Å) is indicative of a multiple bond, moreover; the bond angle N-Ru-N is 150.8°with the nitride bond being bent outside the pincer plane. The major transformation in the reaction between **2** and the acid occurs at the Ru-N site, as such we find it important to illustrate the bonding orbitals involved in the reaction. We start by showing the electronic structure of **2** in Figure 2.10. According to the NBO analysis, the Ru-N bond is characterized as a triple bond with 3 NBOs representing this multiple bond. Intuitively, one would assume a "classical" bonding interpretation of these orbitals, assuming the triple bond to be constituted of a σ and 2 π bonds. While one σ and one π bonds are clearly shown, the other NBO seems to be a hybrid performing an ambiguous type of interaction.
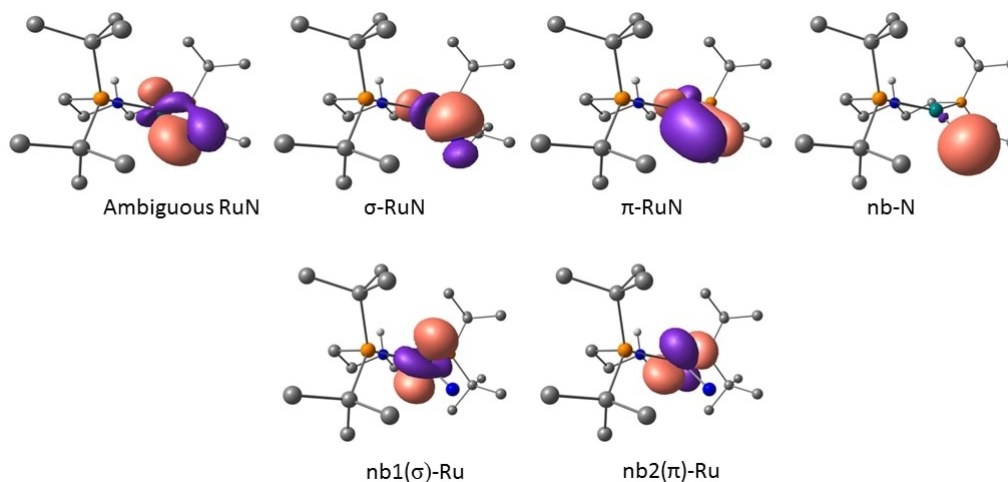
Figure 2.10: Selected natural bonding orbitals of **2**. The hydrogens on the carbons were omitted for clarity. The labels refer to the bonding type shown, where nb refers to non-bonding orbitals.

The analysis reveals the orbitals that are involved in the bonding interaction. The data is as follows:

Ambiguous RuN:
$\phi_{Ru} = 0.14(5s) + 0.73(4d_{xy}) + 0.62(4d_{x^2-y^2}) - 0.25(4d_{z^2})$
$\phi_N = 0.18(2s) - 0.38(2p_x) + 0.91(2p_y)$

σ RuN:
$\phi_{Ru} = 0.42(5s) + 0.29(4d_{xy}) - 0.66(4d_{x^2-y^2}) - 0.54(4d_{z^2})$
$\phi_N = 0.37(2s) - 0.88(2p_x) + 0.29(2p_y)$

π RuN:
$\phi_{Ru} = -0.23(5s) + 0.57(4d_{xz}) - 0.76(4d_{yz})$
$\phi_N = -1.00(2p_z)$

nb N:
$\phi_N = 0.91(2s) - 0.28(2p_x) - 0.30(2p_y)$

nb1σ Ru:
$\phi_{Ru} = -0.60(4d_{xy}) + 0.40(4d_{x^2-y^2}) - 0.67(4d_{z^2})$

nb2π Ru:
$\phi_{Ru} = 0.80(5d_{xy}) + 0.60(5d_{x^2-y^2})$

The shape of the ambiguous NBO could be attributed to the bent geometry of

the terminal nitride. In order to confirm, we decided to run the same analysis on **2** but with the terminal nitride being linear instead. Figure 2.11 shows NBOs of the linear Ru-N bond. **2***.
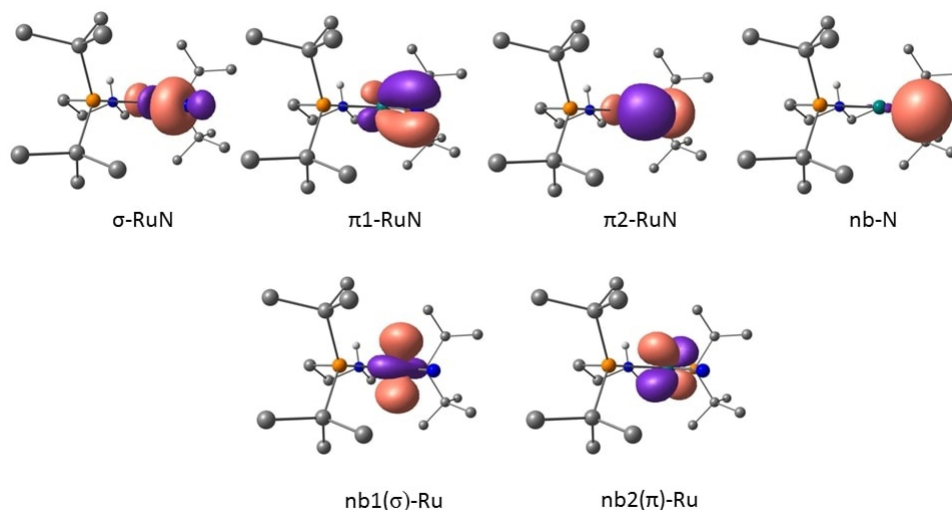
Figure 2.11: The Ru-N natural bonding orbitals of **2***.

A "classical" bonding is observed for the ruthenium nitride bond, showing a σ and 2 π bonds. The N-Ru-N bond angle is the only observed difference between the structures of **2** and **2***. Clearly the orientation of the nitride in the complex has an impact on the NBO topology. The calculated conformational energy for the bending of the Ru-N bond is 1.2 Kcal/mol $\Delta G(2^*-2)$, suggesting that both geometries are accessible under the same conditions. Finally we compare the compositions of the NBOs for both structures to highlight the difference in the electronic structure. The following are the NBO compositions of **2***:

σ RuN:
$\phi_{Ru} = 0.51(5s) - 0.65(4d_{x^2-y^2}) - 0.54(4d_{z^2})$
$h_N = 0.44(2s) - 0.13(2p_x) + 0.89(2p_y)$

$\pi 1$ RuN:
$\phi_{Ru} = 0.99(4d_{xy})$
$\phi_N = -0.99(2p_x)$

$\pi 2$ RuN:
$\phi_{Ru} = -0.45(5p_z) + 0.89(4d_{yz})$
$\phi_N = -1.00(2p_z)$

nb N:
$$\phi_N = 0.90(2s) - 0.44(2p_y)$$

nb1σ Ru:
$$\phi_{Ru} = 0.71(4d_{x^2-y^2}) - 0.67(4d_{z^2})$$

nb2π Ru:
$$\phi_{Ru} = 1.00(4d_{xz})$$

By comparing the composition of each NBO, we learn that the ambiguous RuN NBO of **2** is similar to σ RuN of **2***. The hybrid orbital in the bent structure has one additional valence orbital in its composition namely the $(4d_{xy})$. The role of this extra orbital is to compensate for the orbital interactions with the nitride due to the bent structure, giving a σ type interaction. The second set of NBOs (σ on **2** and $\pi1$ on **2***) are very different form each other. In some sense, the ambiguous NBO in **2** was an interaction between the metal hybrid orbital and the nitrogen (p_y). This mode of interaction is replicated for the interaction of the metal hybrid orbital with the orthogonal but similar nitrogen (p_x). For the linear structure however, $\pi1$ RuN is clearly a π bond resulting from the interaction between $4d_{xy}$ and $2p_x$. This sums up the major differences between the bent **2** and the linear **2*** structures with regards to the bonding interactions.

The reaction pathway begins with the reaction between 2 and benzoic acid, pass through a transition state **TS1** as shown in Figure 2.8. The Ru-N bonding NBOs of TS1 are shown in Figure 2.12. The major observation is the similarity of the electronic structure between **TS1** and **2***. The analysis points towards a linear Ru-N bond when the addition of the acid is taking place. This observation was verified by calculating the intrinsic reaction coordinate shown in Figure 2.13. As the acid approaches, the Ru-O bond as well as the N-H bonds become shorter. This bond shortening process is coupled with an increase in the N-Ru-N bond, suggesting that the transition state and the activation of the ruthenium nitride bond takes place on a linear bond.

The compositions of the selected NBOs are laid out as follows:

σ RuN:
$$\phi_{Ru} = 0.34(5s) - 0.29(4d_{xy}) + 0.80(4d_{x^2-y^2}) - 0.39(4d_{z^2})$$
$$\phi_N = 0.38(2s) + 0.92(2p_x)$$

Ambiguous RuN:
$$\phi_{Ru} = 0.38(5s) + 0.37(5p_y) + 0.19(4d_{x^2-y^2}) + 0.46(4d_{z^2})$$
$$\phi_N = -0.99(2p_y)$$
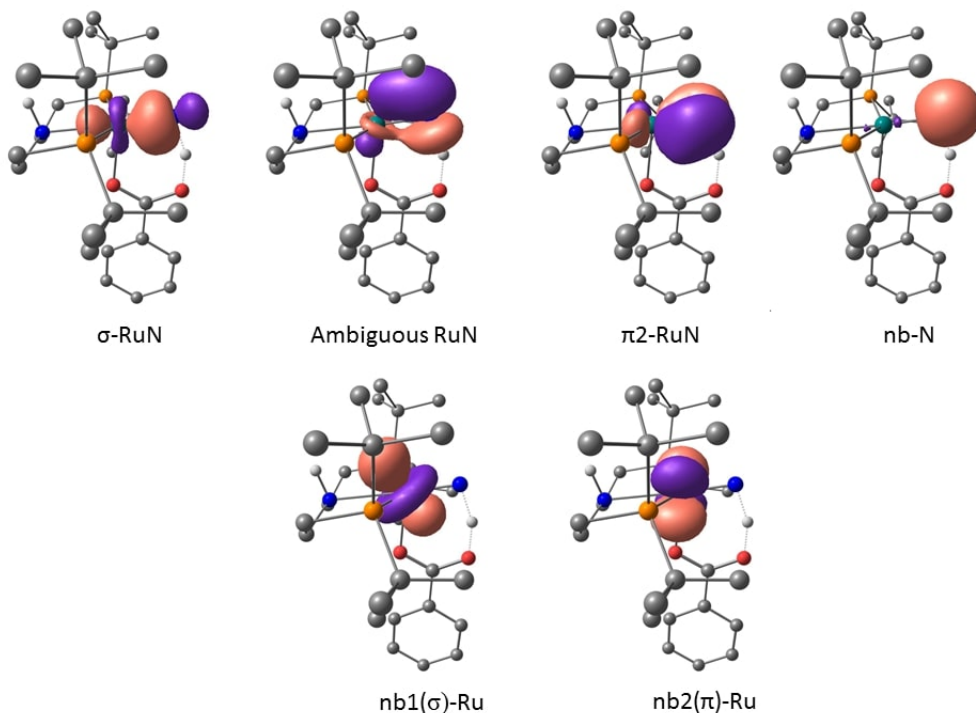
Figure 2.12: Selected NBOs of **TS1**.

π2 RuN:
$\phi_{Ru} = -0.46(5p_z) + 0.86(4d_{xz})$
$\phi_N = -1.00(2p_z)$

nb N:
$\phi_N = 0.92(2s) - 0.38(2p_x)$

nb1σ Ru:
$\phi_{Ru} = 0.71(5p_y) - 0.64(4d_{xy}) - 0.54(4d_{x^2-y^2}) - 0.53(4d_{z^2})$

nb2π Ru:
$\phi_{Ru} = 1.00(4d_{xz}) + 0.97(4d_{yz})$

The ambiguous RuN NBO shows an additional $(5p_y)$ contribution from the metal compared to the ambiguous RuN NBO of **2**. The additional $(5p_y)$ orbital is interacting with the nitrogen's $(2p_y)$ as is evident from the composition analysis. The emergence of this new metal atomic orbital in the hybrid metal NBO can be attributed to the incoming proton of the acid, in addition to the impact of polarizing the orbitals in order to form a new σ NH bond.
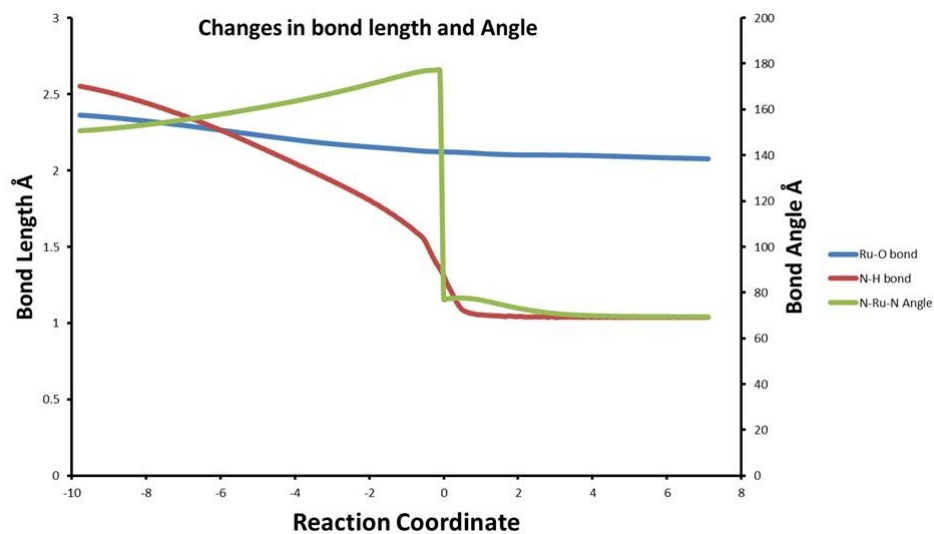
Figure 2.13: The intrinsic reaction coordinate for the reaction between **2** and benzoic acid. The changes in the bond lengths and bond angle are shown.

The addition of the benzoic acid will lead to the formation of a κ-1 imido intermediate **i1**. The N-Ru-N angle is 170°, with the imido bent away from the coordinated acid. The NBOs of the Ru-N bond along with their lone pairs are shown in Figure 2.14.
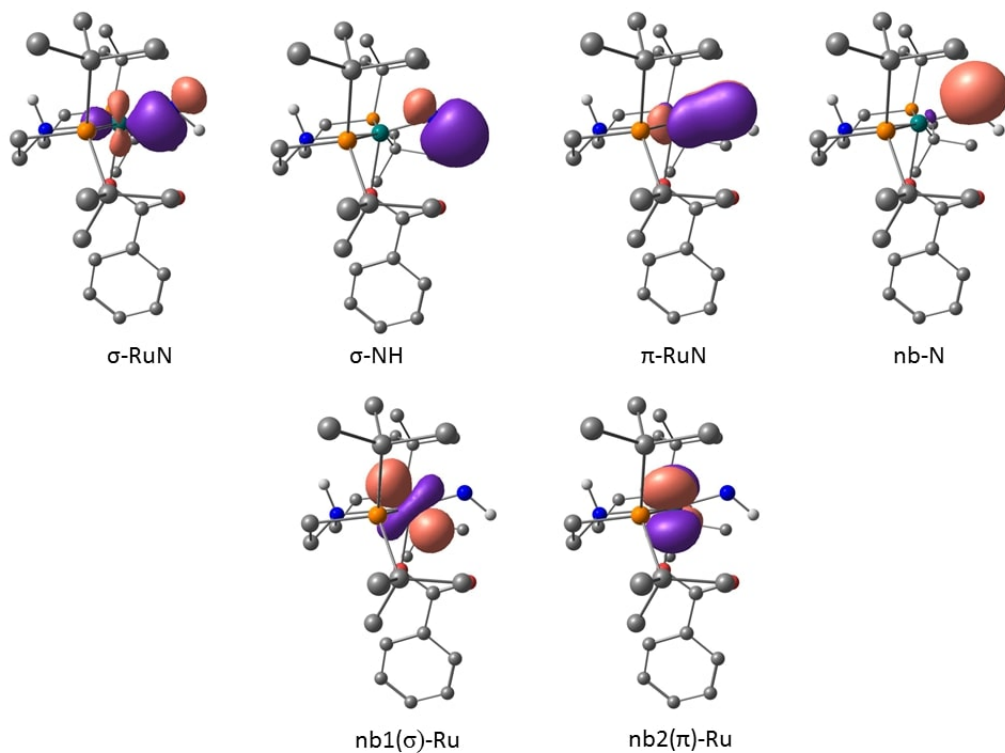
Figure 2.14: Selected NBOs of **i1**.

The compositions of the selected NBOs are laid out as follows:

  σ RuN:
$\phi_{Ru} = 0.18(5s) - 0.16(4d_{xy}) + 0.93(4d_{x^2-y^2}) + 0.26(4d_{z^2})$
$\phi_N = -0.38(2s) + 0.53(2p_x) - 0.76(2p_y)$

  σ NH:
$\phi_N = 0.42(2s) + 0.63(2p_x) + 0.65(2p_y)$
$\phi_H = -1.00(1s)$

  π RuN:
$\phi_{Ru} = 0.42(6p_z) + 0.42(7p_z) + 0.83(4d_{yz})$
$\phi_N = -1.00(2p_z)$

  nb N:
$\phi_N = 0.82(2s) + 0.57(2p_x)$

  nb1σ Ru:
$\phi_{Ru} = 0.88(4d_{xy}) + 0.28(4d_{x^2-y^2}) - 0.37(4d_{z^2})$

nb2π Ru:
$$\phi_{Ru} = 1.00(4d_{xz})$$

The σ RuN shows a slight bending on the same plane of the newly formed σ NH bond axis. This is attributed to the additional contribution form the nitrogen's $(2p_y)$ orbital to the σ RuN NBO. The selected NBOs show similar compositions and topology to **TS1** except for the transformation of the ambiguous RuN on **TS1** into a σ NH bond on **i1**. The NBOs that stayed the same as the reaction occurred rule out their involvement in the reaction.

The benzoic acid moiety undergoes a second coordination step forming the second intermediate **i2**.Two simultaneous events occur, the uncoordinated oxygen binds to the metal center and the metal imido bond rotates resulting in a N-Ru-N bond of 78°.The NBOs of the Ru-N bond along with their lone pairs are shown in Figure 2.15.

σ-RuN σ-NH π-RuN nb-N

nb1(σ)-Ru nb2(π)-Ru
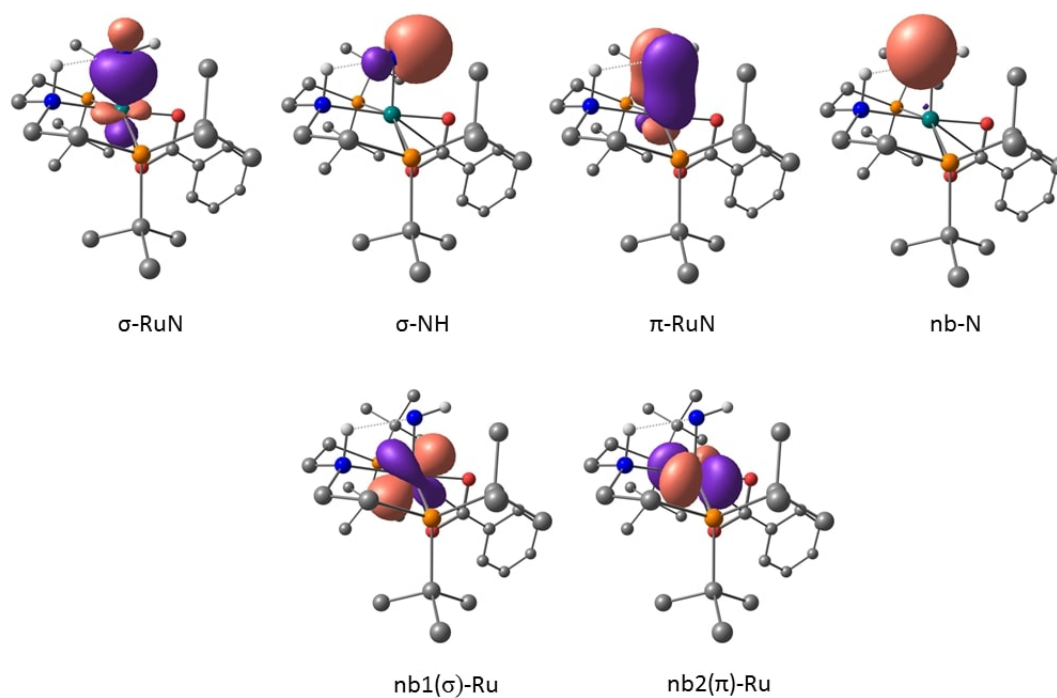
Figure 2.15: Selected NBOs **i2**.

The major change in NBO topology from **i1** to **i2** is the directionality of the orbitals involved. This is evident from the compositions of the **i2** NBOs. In the

σ RuN NBO the contribution of the $(4d_{x^2-y^2})$ is eliminated and the $(4d_{xy})$ orbital becomes the major contributor in the ϕRu. The shuffling of the NBO contributing orbitals is evident in nb2π Ru where the participating orbitals completely change from **i1** to **i2** as is shown in the composition analysis.

σ RuN:
$$\phi_{Ru} = 0.24(5s) + 0.91(4d_{xy}) + 0.30(4d_{z^2})$$
$$\phi_{N} = -0.46(2s) + 0.66(2p_x) - 0.59(2p_y)$$

σ NH:
$$\phi_{N} = 0.47(2s) + 0.74(2p_x) + 0.47(2p_y)$$
$$\phi_{H} = 1.00(1s)$$

π RuN:
$$\phi_{Ru} = -0.35(6p_z) + 0.32(7p_z) + 0.73(4d_{xz}) - 0.46(4d_{yz})$$
$$\phi_{N} = 1.00(2p_z)$$

nb N:
$$\phi_{N} = 0.76(2s) - 0.65(2p_y)$$

nb1σ Ru:
$$\phi_{Ru} = 0.22(4d_{xy}) + 0.94(4d_{x^2-y^2}) - 0.26(4d_{z^2})$$

nb2π Ru:
$$\phi_{Ru} = 0.53(4d_{xy}) + 0.85(4d_{yz})$$

The next step in the reaction pathway concerns the transfer of a proton from the pincer nitrogen on the imido nitrogen. The NBOs of both the transition state (**TS2**) and the intermediate formed (**i3a**) are shown in Figures 2.16-2.17.

The σ RuN NBO retains its composition in the transition state in addition to acquiring a an extra $(4d_{x^2-y^2})$ contribution. The σ NH NBO shows no change as the transition state is proceeding towards the new intermediate. The π RuN NBO loses some of its d-character and gains some p-character. This could be due to approach of the incoming proton from the pincer backbone. Only nb2π Ru shows a change in its composition by switching into the $(4d_{xy})$ into $(4d_{xz})$ orbital.
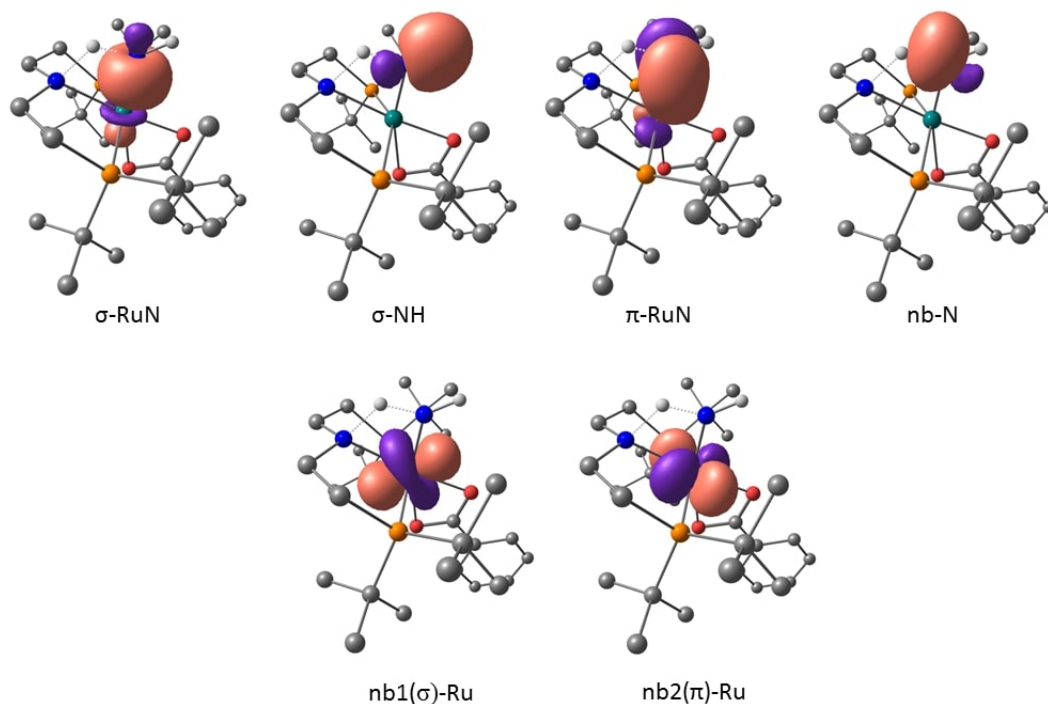
Figure 2.16: Selected NBOs of **TS2**.

The compositions of the selected NBOs on **TS2** are as follows:

σ RuN:
$\phi_{Ru} = 0.24(5s) + 0.91(4d_{xy}) + 0.27(4d_{x^2-y^2}) + 0.30(4d_{z^2})$
$\phi_N = -0.57(2s) + 0.61(2p_x) + 0.55(2p_y)$

σ NH:
$\phi_N = 0.48(2s) - 0.79(2p_x) + 0.38(2p_y)$
$\phi_H = 1.00(1s)$

π RuN:
$\phi_{Ru} = 0.46(5p_z) - 0.30(4d_{yz})$
$\phi_N = 1.00(2p_z)$

nb N:
$\phi_N = 0.67(2s) - 0.74(2p_y)$

nb1σ Ru:
$$\phi_{Ru} = -0.49(4d_{xy}) + 0.81(4d_{x^2-y^2}) - 0.32(4d_{z^2})$$

nb2π Ru:
$$\phi_{Ru} = 0.34(4d_{xz}) + 0.94(4d_{yz})$$

σ-RuN σ1-NH σ2-NH π-RuN

nb1(σ)-Ru nb2(π)-Ru
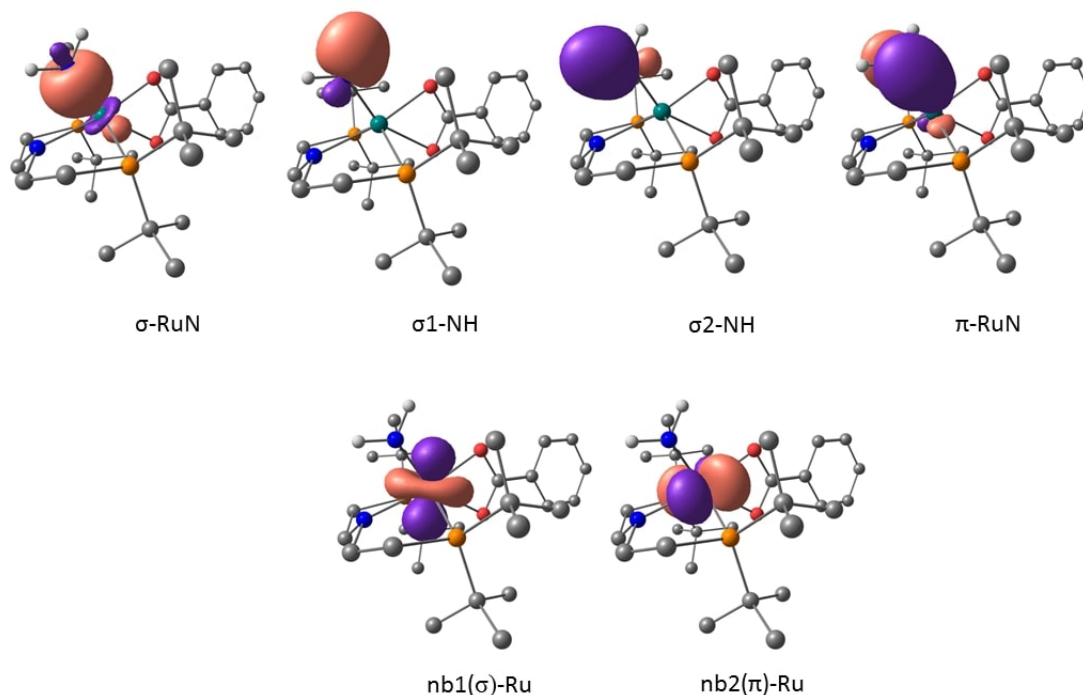
Figure 2.17: Selected NBOs of **i3a**.

The formation of the **i3a** intermediate brings along the formation of a new σ NH bond. The nature of the σ RuN NBO changes slightly by adopting an increased z-character due to the new $(4d_{yz})$ contribution and the loss of the $(4d_{xy})$ and $(4d_{x^2-y^2})$ orbitals in its composition. On the other hand the π RuN shows a loss of z-character and gains an x-character composition NBO by the interaction between $(5p_x)$ and $(2p_x)$. We also observe a switch in the orbitals involved in the non-bonding orbitals of ruthenium. The NBO composition analysis clearly shows a changing electronic structure, that is shuffling between z-directed orbitals and x,y-directed orbitals to accommodate the newly formed σ NH bond. Finally, it is important to notice the lack of a lone pair on the nitrogen and it forming 4 bonds (two with the metal and two with the protons). It is not clear how the nitrogen adopts such a structure, however, according to the mechanism illustrated in Figure 2.8, this intermediate exhibits a high energy across the potential energy

surface of the reaction, and that it is further lowered by proceeding towards the low energy isomer **i3b**.

σ RuN:
$\phi_{Ru} = 0.44(5s) + 0.68(4d_{yz}) + 0.54(4d_{z^2})$
$\phi_N = -0.57(2s) + 0.61(2p_x) + 0.55(2p_y)$

σ1 NH:
$\phi_N = 0.54(2s) + 0.48(2p_x) - 0.67(2p_z)$
$\phi_H = 1.00(1s)$

σ2 NH:
$\phi_N = -0.54(2s) + 0.81(2p_y)$
$\phi_H = -1.00(1s)$

π RuN:
$\phi_{Ru} = 0.55(5p_x)$
$\phi_N = 0.96(2p_x)$

nb1σ Ru:
$\phi_{Ru} = 0.55(4d_{yz}) - 0.78(4d_{z^2})$

nb2π Ru:
$\phi_{Ru} = -0.90(4d_{xy}) - 0.36(4d_{x^2-y^2})$

A barrier-less rotation follows the formation of **i3a**, giving the energetically favored rotamer **i3b**. The orbital composition of the selected NBOs and listed and they show no major change in the σ RuN bond. We observe the rearrangement of the σ2 NH bond, in accordance to the rotation of the RuN moiety. The change in directionality is also observed for the π RuN bond much like the latter. Interestingly, the NBOs of both non-bonding Ru show a similar composition by using the same orbitals, however, the major difference lies in the coefficient of each orbital which is dramatically observed in the figure. Moreover the nature of the first non-bonding orbital (nb1) is no longer σ but adopts a π type non-bonding NBO.

σ RuN:
$\phi_{Ru} = 0.44(5s) + 0.50(4d_{yz}) + 0.71(4d_{z^2})$
$\phi_N = 0.61(2s) + 0.54(2p_y) + 0.58(2p_z)$

σ1 NH:
$\phi_N = 0.55(2s) + 0.72(2p_x) - 0.40(2p_z)$
$\phi_H = 1.00(1s)$
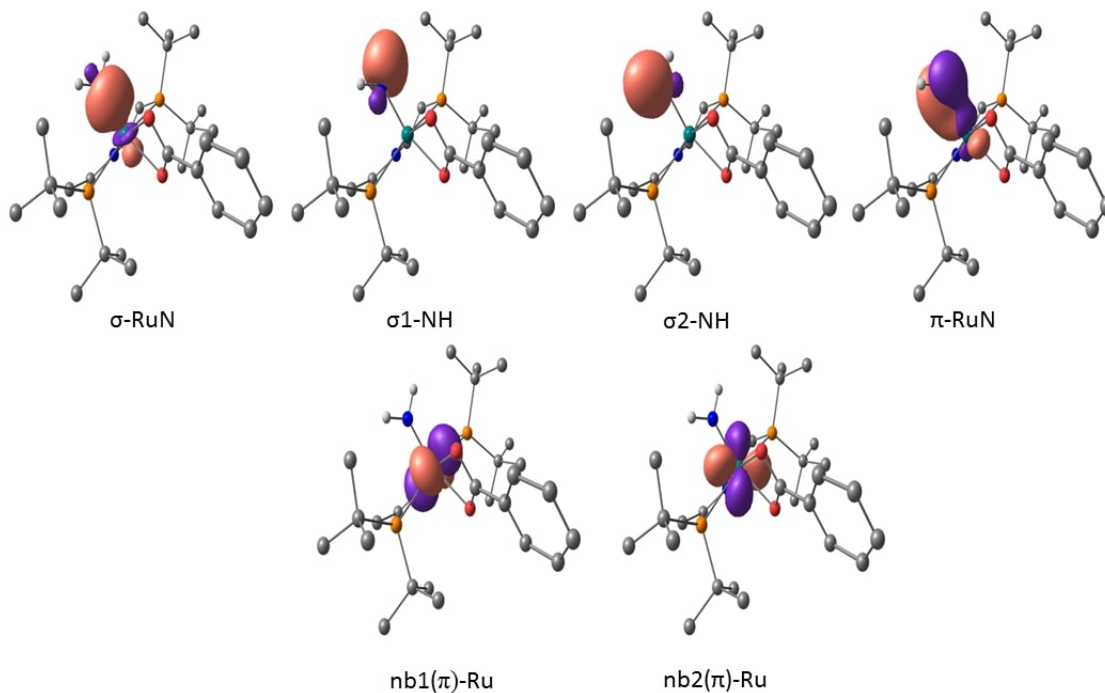
Figure 2.18: Selected NBOs of **i3b**.

$\sigma 2$ NH:
$\phi_N = 0.54(2s) - 0.70(2p_x) - 0.43(2p_z)$
$\phi_H = -1.00(1s)$

π RuN:
$\phi_{Ru} = 0.54(4d_{yz}) - 0.50(4d_{z^2})$
$\phi_N = -0.81(2p_y)$

nb1π Ru:
$\phi_{Ru} = 0.67(4d_{xy}) + 0.74(4d_{xz})$

nb2π Ru:
$\phi_{Ru} = 0.73(4d_{xy}) + 0.67(4d_{xz})$

Finally a PCET step takes place resulting in the formation of the ammine product **3**. This step involves a transition state **TS3**, where a proton and two electrons are transferred from the pincer. The selected NBOs are shown in Figures 2.19-2.20.
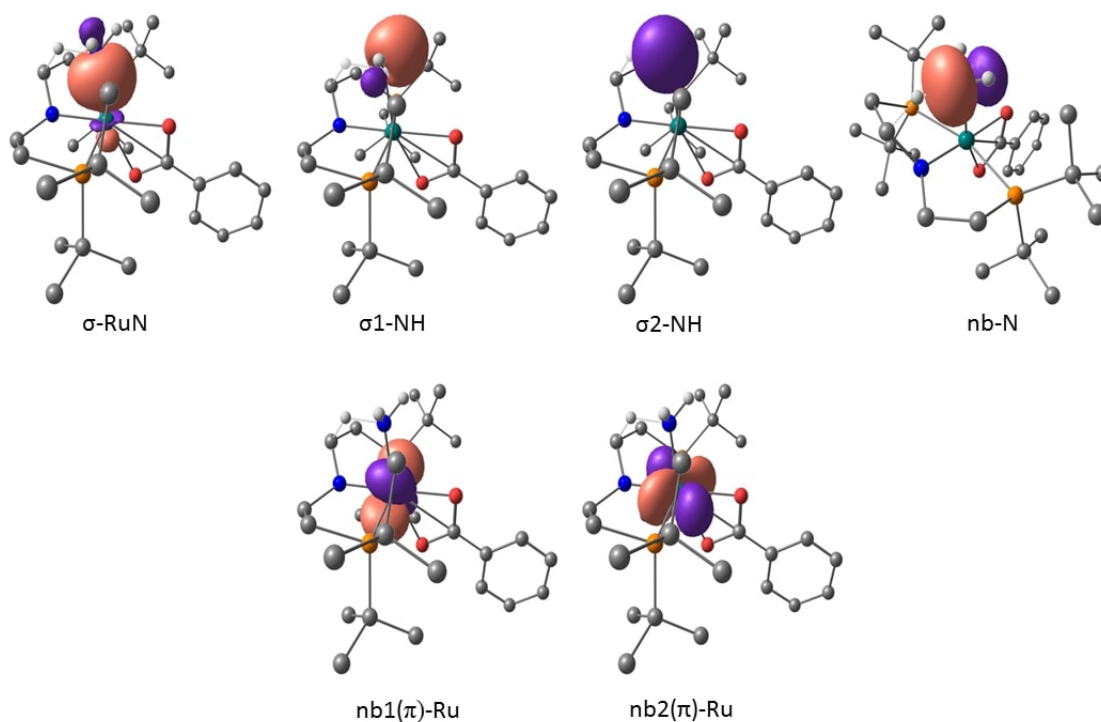
Figure 2.19: Selected NBOs of **TS3**.

The transition state NBO composition shows the loss of the π character between the ruthenium and the newly protonated amide nitrogen, and the resurgence of the lone pair on the same nitrogen. The orientation of this lone pair lies in the same plane from which the last proton will be transferred.

σ **RuN**:
$$\phi_{Ru} = 0.62(4d_{yz}) + 0.48(4d_{z^2})$$
$$\phi_N = 0.55(2s) + 0.83(2p_y)$$

σ**1 NH**:
$$\phi_N = 0.52(2s) + 0.65(2p_x) - 0.55(2p_z)$$
$$\phi_H = 1.00(1s)$$

σ**2 NH**:
$$\phi_N = -0.52(2s) + 0.73(2p_x) + 0.40(2p_z)$$
$$\phi_H = -1.00(1s)$$

nb N:

$$\phi_N = -0.76(2p_y) + 0.47(2p_z)$$

nb1π Ru:
$$\phi_{Ru} = -0.95(4d_{xz})$$

nb2π Ru:
$$\phi_{Ru} = 0.92(4d_{xy})$$
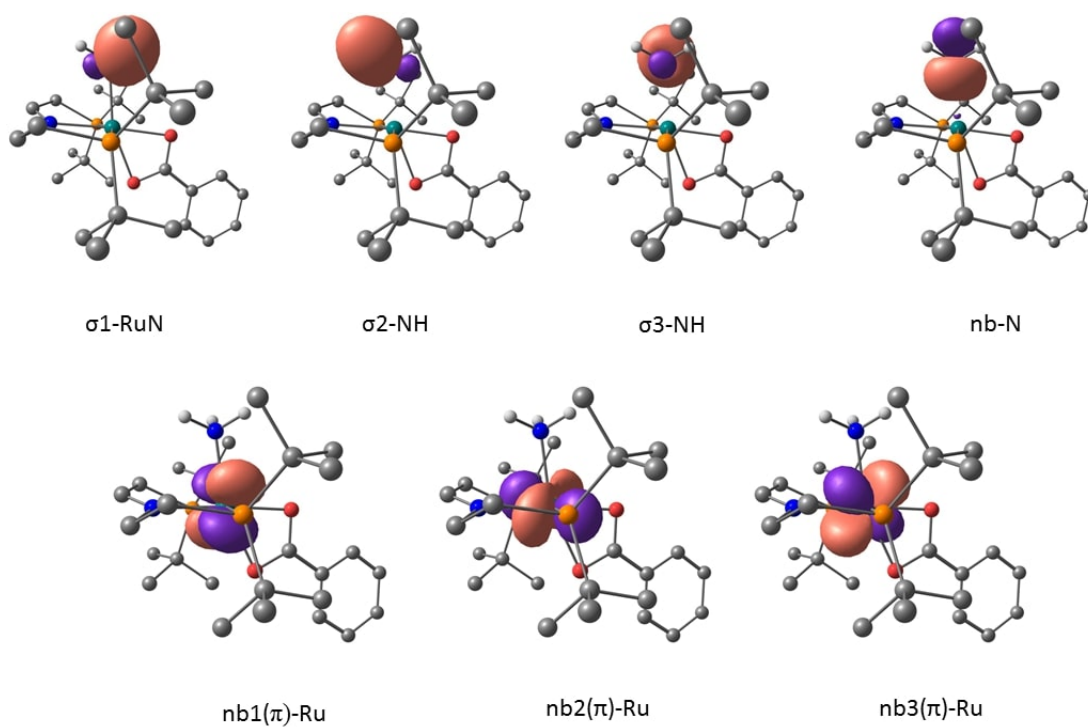
Figure 2.20: Selected NBOs of **3**.

The composition of the selected NBOs of **3** reveals the absence of a σ bond connected ruthenium and the ammine nitrogen. This in turn results in the emergence of two non-bonding NBOs, one on the metal and the other on the nitrogen. This observation speaks of the dissociative character of the Ru-N bond in the product **3**.

σ1 NH:
$$\phi_N = 0.51(2s) - 0.56(2p_x) - 0.56(2p_z)$$
$$\phi_H = 1.00(1s)$$

$\sigma 2$ NH:
$\phi_N = 0.50(2s) - 0.77(2p_y)$
$\phi_H = -1.00(1s)$

$\sigma 3$ NH:
$\phi_N = 0.52(2s) + 0.78(2p_x)$
$\phi_H = -1.00(1s)$

nb N:
$\phi_N = -0.71(2p_z)$

nb1π Ru:
$\phi_{Ru} = 0.92(4d_{xz})$

nb2π Ru:
$\phi_{Ru} = 0.77(4d_{xy})$

nb3π Ru:
$\phi_{Ru} = 0.81(4d_{z^2})$

The NBO analysis reveals the types of bonds being broken and formed during the transformations. In step 1, as the reaction occurs between **2** and benzoic acid giving the κ^1 intermediate **i1**, we observe a breaking of one RuN bond and the formation of a NH bond. The lone pair on the nitride nitrogen does not participate in the interaction. In step 2, the orbital of the lone pair on the nitrogen of **i2** receives the proton from the backbone nitrogen forming the **i3a** intermediate, revealing a fundamentally different interaction in the electronic structure. In the **i3a** intermediate we noted the formation of four bonding interaction on the amide nitrogen, namely two bonds with Ru ($\sigma and \pi$) and two σ NH bonds. In step 3, when the ammine product **3** forms we notice the absence of any bonding interaction between Ru and the ammine nitrogen, and the resurgence of the lone pair on the nitrogen and the appearance of a new non-bonding orbital on the metal, effectively changing its oxidation state from (IV) to (II). The last proton transfer from the pincer carbon results in the breaking of both the $\sigma and \pi$ bonds between the metal and the nitrogen. These observations speak of unique electronic structure changes for each proton transfer step.

2.5.2 AIM Charges

The quantum theory of atoms in molecules (QTAIM) describes a chemical system based on its electron density distribution function $\rho(r)$[24]. The topology of the electron density is used to define chemical bonding and other atomic properties in the molecule. For the purpose of this work, we have utilized the AIMALL program in order to calculate the atomic charges of all the species involved in the reaction mechanism. This method is considered the most reliable to compute accurate atomic charges in a complex or a molecule. In Figure 2.21 we have tabulated the charges of all the species in the reaction pathway.

AIM Charges									
Species	**2**	**TS1**	**i1**	**i2**	**TS2**	**i3a**	**i3b**	**TS3**	**3**
Ru	0.7	1.0	1.0	1.1	1.1	1.1	1.3	1.1	0.9
Nitride	-0.5	-0.8	-0.8	-0.8	-0.9	-0.9	-1.0	-0.9	-0.9
Pincer N	-0.9	-0.9	-0.9	-0.9	-1.0	-0.9	-0.9	-0.9	-1.1
H-transfer		0.5	0.4	0.4	0.5	0.4	0.0	0.2	0.3

Figure 2.21: Calculated QTAIM charges for ruthenium, nitride, pincer nitrogen and the protons being transferred.

The charges associated with Ru (+0.7) and nitride nitrogen (-0.5) on the starting complex **2** implicate a covalent character to this bond. Formally, a nitride ligand would exhibit a (-3) charge which would be consistent with the NBO analysis; however, we observe a lowered charge magnitude of (-0.5). The discrepancy in the charge magnitude offers an important insight into the interaction between the nitride and the ruthenium which is the only atom attached to it. The data predicts charge depletion on the nitride moiety once it is bonded to the metal. A major change in charge is observed upon the reaction between **2** and benzoic acid. The metal charge becomes more positive while the nitride nitrogen becomes more negative. The pincer nitrogen on the other hand does not undergo any change in the magnitude of its negative charge across the reaction. We can conclude from the data the major change in the system occurs in the first step where the benzoic acid reacts with our complex causing a change in $\rho(r)$. Furthermore, the comparable charge magnitudes between **TS1** and **i1** reflects the position of the transition state on the potential energy surface of the reaction and suggests that **TS1** is a late transition state. As such an in-depth investigation of the transition state **TS1** can give us insight into the chemistry required to activate metal nitride bonds for the process of developing novel ammonia synthesis methods. Another noteworthy change in the charge is related to the proton transferred in step three. The proton in intermediate **i3b** is located on the pincer carbon, and has a neutral

charge as expected for a C-H bond hydrogen. The hydrogen when transferred (**TS3**) gains a positive value characteristic of a proton, which is representative of the PCET step.

2.6 Structure-Activity Study as a Function of the Benzoic Acid Derivative and Metal Center

2.6.1 Effect of Varying the Benzoic Acid Derivative

Bifunctional addition of benzoic acid to the RuN bond of **2** means there are two components for the reaction, protonation transfer and ligand coordination. The computed intrinsic reaction coordinate of addition is most consistent with a concerted transformation. This condition raises interesting fundamental questions on the sensitivity of the kinetics and thermodynamics of the given step on the nature of the coordinating acid. For example, increased acidity of the acid should obviously make the proton transfer component more favorable. However, the dependence of the reaction rates and energies on accompanying ligand coordination component are less clear. To better understand this step, we conduct a detailed structure activity-study in which we vary the substituents on the benzoic acid. We limit the study to substitution at the para-position which exerts effects primarily by inductive effects.

In physical organic chemistry, the hammett plot is a type of linear free energy relationship analysis used to give chemically relevant information about the electronic effect of the substituents on aromatic systems [25]. The Hammett parameters are often used to construct plots relating a reaction parameter (such as activation energy or reaction energy) to the effect of changing a substituent on a reactant. Accordingly, we considered substituents that vary considerably in the σ_p parameter, namely: OH (-0.37), OMe (-0.27), NO_2 (0.78) Cl (0.23) ^{t}Bu (-0.20) CH_3(-0.17) F (0.06) CN (0.66) [26]. The two limiting pK_a values in this series are 21 and 25, respectively for X = NO_2 and CH_3, respectively [27].

The computed activation and reaction energies for addition of the substituted benzoic acids are given in Figure 2.22.

Remarkable, the plot reveals near total absence of substituent effects on the rates of benzoic acid addition. For example, the activation energies for X = OH and NO_2 are, 17.8 and 17.9, kcal/mol, respectively. The thermodynamics of the addition reaction shows increased dependence on X, but the dependence is very small. For example, for X = OH and NO_2, ΔG = 6.4 and 4.4 kcal/mol, respectively.

Typically the slope in a hammett plot can have implications on the type of mechanism taking place in a reaction [28]. Predictions can be made on whether the reactant is acting as nucleophile or an electrophile, and whether specific type of
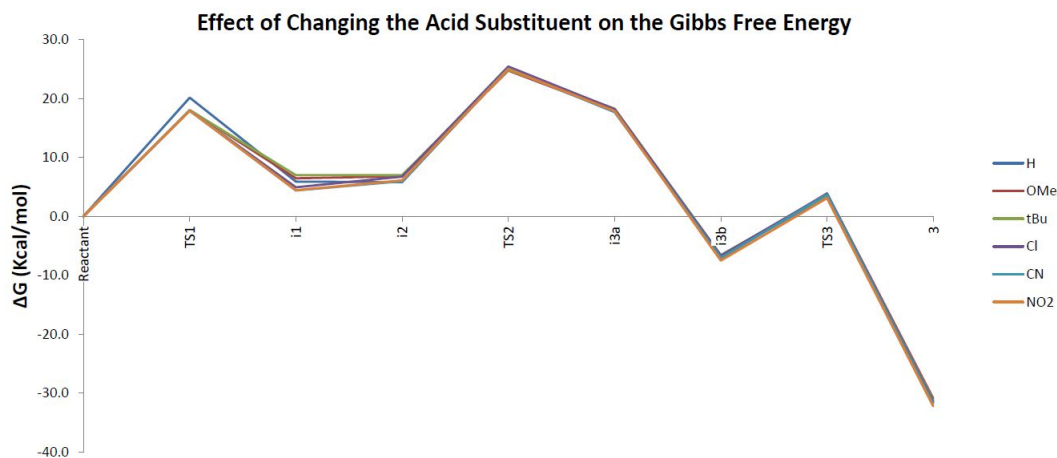
Figure 2.22: Computed activation and reaction energies for the addition of the substituted benzoic acids to **2**.
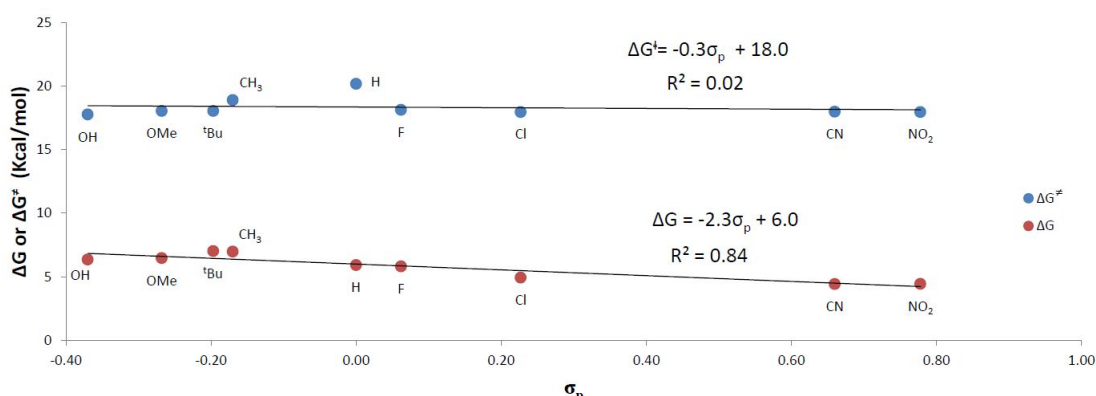
Figure 2.23: Hammett plot of step one in the reaction between substituted benzoic acid and **2**.

activation mechanism is taking place. For such information to be extracted from a hammett plot the magnitude and sign of the slope would be indicative of the relation between the free energy and the dissociation (protonation) energy of the acid represented by the hammett parameter. In the case of the activation energy, we observe a slope of -0.3 signifying that changing the substituent on the acid will have no impact on the rate of the reaction. Regarding, the reaction energies, we report a slope of -2.2, representing a weak impact of changing the acid substituent on the thermodynamics of the reaction. A slope of -2.3 informs us that the more acidic 4-nitrobenzoic acid will slightly favor the formation of the first intermediate i1.

To better understand the lack of substituent effects on the thermodynamics of the given bifunctional addition step, we break the computed net reaction energies into a thermodynamic cycle with two components as outlined in Figure 2.24.
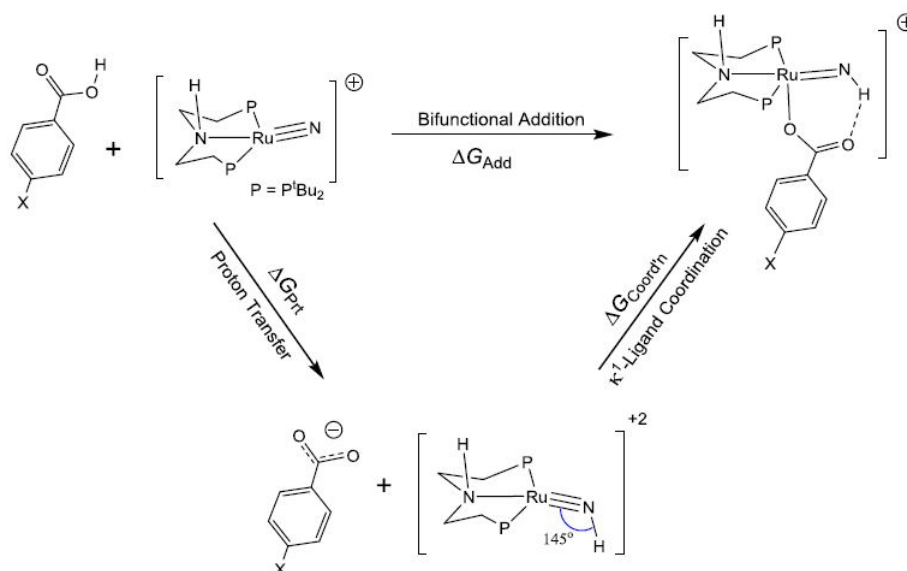
Figure 2.24: A devised reaction cycle representing the reaction between the acids and **2** giving the κ^1-intermediate **i1**.

The first component is a proton transfer step from the benzoic acid derivative to the nitrido ligand of **2**. The energy of this step is denoted ΔG_{Prt}. The second step in the cycle is κ^1-coordination of the benzoate derivative to the protonated nitride complex to give intermediate **i1**. The energy of this step is denoted $\Delta G_{coord'n}$. The results are given schematically in Figure 2.25. The absolute energies of ΔG_{Prt} are in the 40 kcal/mol range. This can be attributed to the inherent difficulty of the nitride to be protonated as well as to the original positive charge on the given RuN complex which leads to a dicationic protonated product. However, the computed trends in ΔG_{Prt} clearly show a pronounced dependence on the nature of the carboxylic acid. For example, for X = OH and NO_2, ΔG_{Prt} = 42.9 and 35.2 kcal/mol, respectively. Note that the given calculations are computed in a THF continuum. The variations in the acidity of related organic molecules in these solvents can be more pronounced than in water. This is called a damping solvent effect.

Figure 2.25 shows the computed absolute values for the coordination energies $\Delta G_{coord'n}$ to be in the 35 kcal/mol range. These highly favored energies are driven in part because of the charge combination between a cation and an anion, and in part because of the formation of two bonds, a classical bond due to
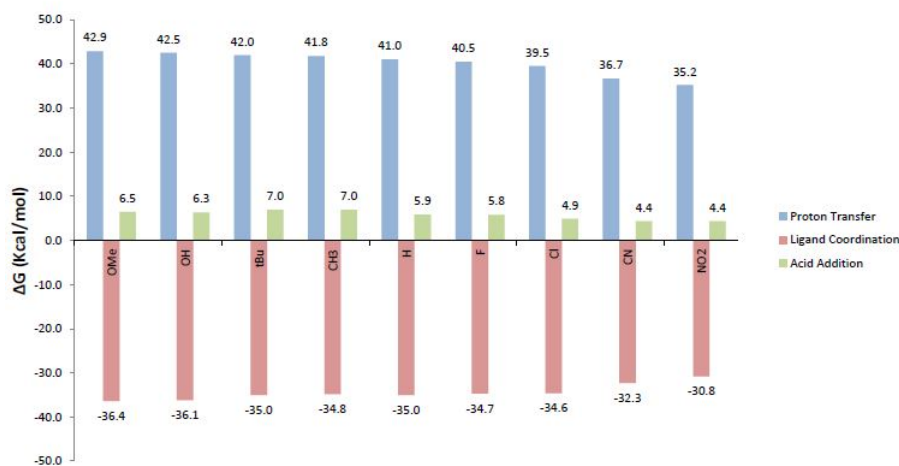
Figure 2.25: Column graph representing the energy steps in the devised cycle for the first step of the mechanism.

κ^1-coordination of one benzoate oxygen and the metal, and a hydrogen bond between the proton on the nitride and the second benzoate oxygen. Again, the data in Figure 2.25 show a pronounced dependence of $\Delta G_{coord'n}$ on the substituent X. Benzoate anion derivative with an electron withdrawing groups bind less effectively than anions with an electron donating one. For example: $\Delta G_{coord'n}$ for X = OMe and NO$_2$ are -36.4 and -30.8 kcal/mol respectively. The opposite effects of X on ΔG_{Prt} and $\Delta G_{coord'n}$ is not unexpected, but to have the two effects quantitatively opposite is, by all measures, rather remarkable.

Another feature to be analyzed in Figure 2.25 is the full addition step, which is a result of adding the energies of both steps. The green plots are in the quadrant as the proton affinity step, suggesting that proton transfer step to be the energetically dominant step in this mechanism. This information can be replicated by taking the magnitude of each step, and comparing them. As such we realise that the proton affinity step always has a higher magnitude in comparison to the ligand coordination step, supporting the hypothesis that the acid addition step is dominated by the proton transfer rather than the ligand coordination step.

The cycle energies elucidate the reason behind the nearly equivalent plots in Figure 2.22. While we observe a small difference in energy between the magnitudes of the proton affinity and ligand coordination steps, they also hold opposite signs. The addition of the acid to **2** is concerted, with both steps occurs together, eventually cancelling each other out, with the remainder regarded as the reaction energy. As such we conclude that the step involving the activation of the Ru-N

bond in this novel reaction mode requires a high energy proton transfer coupled with a low energy counter ion coordination, in this case the conjugate base of the proton source.

The large effect of X on $\Delta G_{coord'n}$ for κ^1-coordination is evident in Figure 2.25. As such we became interested in examining the hydrogen bonding element of the coordination. A new cycle, shown in Figure 2.26, is used to compute the hydrogen bonding contribution to the coordination step in the overall bifunctional addition of benzoic acid to **2**.
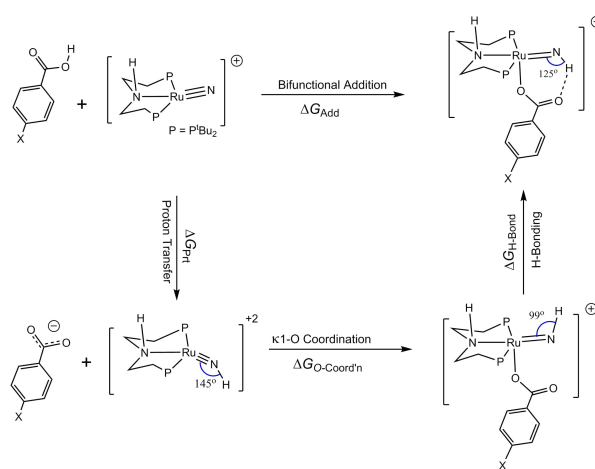
Figure 2.26: A variant cycle representing the reaction between the acids and **2** including the hydrogen bonding contribution of the coordination step.

The step depicting the coordination of the benzoate anion to the protonated complex without the involvement of the hydrogen bonding between the imide nitrogen and the uncoordinated oxygen atom of the acid anion is named κ^1O-coordination and its energy is termed $\Delta G_{O-coord'n}$. The energy of the step involving the formation of the hydrogen bond between the newly transferred proton and the uncoordinated oxygen is called ΔG_{H-Bond}. We observe a change in the bond angle of Ru-N-H (shown in blue) as the benzoate coordinates to the protonated Ru complex from 145° to 99° in the absence of the hydrogen bond and 125° once the hydrogen bonding interaction is involved. Noteworthy, the change in the bond angle from 99° to 125° can be attributed solely to the formation a hydrogen bond in the complex. The computed energies for the steps of the cycle in Figure 2.26 are shown in the column graph of Figure 2.27.

The energies computed for the proton transfer (ΔG_{Prt}) and the complete bifunctional addition of the benzoic acid to form the intermediate **i1** (ΔG_{Add} remain the same since these steps were not changed. We begin by analysing the κ^1O-

34
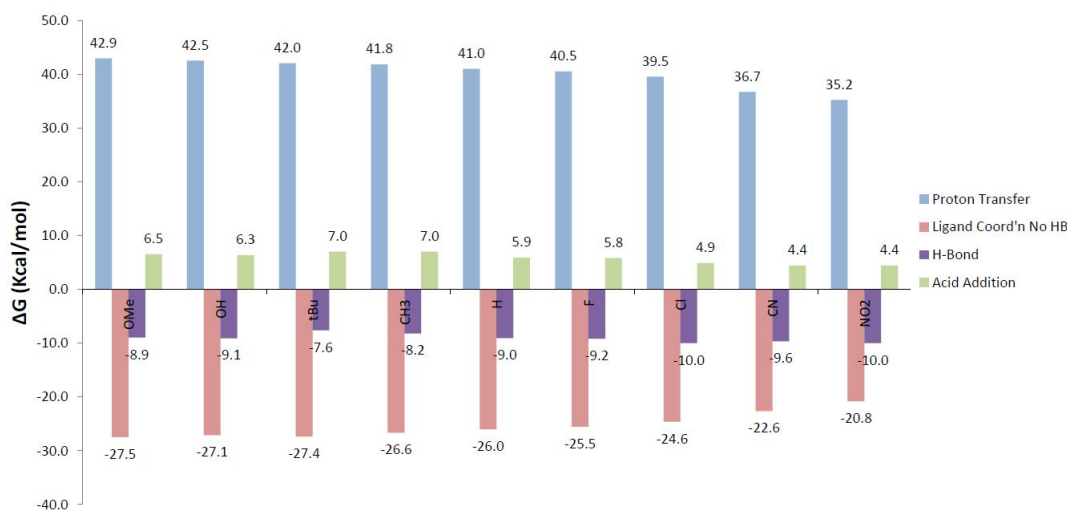
Figure 2.27: A variant cycle representing the reaction between the acids and **2** including the hydrogen bonding contribution of the coordination step.

coordination energies, $\Delta G_{O-coord'n}$. The energies of this step are computed to be within the range of 26 Kcal/mol, which is nearly 10 Kcal/mol higher for the $\Delta G_{coord'n}$ step shown in Figure 2.25. Remarkably, the difference in the coordination step (around 10 Kcal/mol) is accounted for by the hydrogen bonding step ΔG_{H-Bond}. The energies computed for the hydrogen bonding step are fall within the 10 Kcal/mol, and they contribute towards the stabilization of the complex by the same amount. In short, the new cycle allows us to put a number on the stabilization energy afforded by the coordination of the benzoate anion alone without hydrogen bonding (26 Kcal/mol) and the hydrogen bonding component (10 Kcal/mol). These stabilization components of the novel bifunctional addition reaction between benzoic acid and **2** work to compensate for the high energy of protonation (40 Kcal/mol) and in turn activate the seemingly inert ruthenium nitride bond towards the formation of the ammine product.

Given the large effect of X on $\Delta G_{coord'n}$ for κ^1-coordination, we became interested to examine if an even greater effect may be exerted in κ^2-coordination of the given series of benzoate derivatives. For this purpose we consider another cycle shown in Figure 2.28. Apart from the ΔG_{Prt} which remains the same in this cycle, we denote the free energy change by the κ^2 coordination as $\Delta G_{coord'n2}$ and the bifunctional addition to the **i2** intermediate as ΔG_{Add2}.

The computed free energies for the second cycle are shown in Figure 2.29. The κ^2-coordination energies remain within the same range (35 Kcal/mol) as the κ^1-coordination step. Comparing the corresponding acids in both column graphs reveals that the κ^2-coordination energy, $\Delta G_{coord'n2}$, is slightly higher by 1 Kcal/mol.
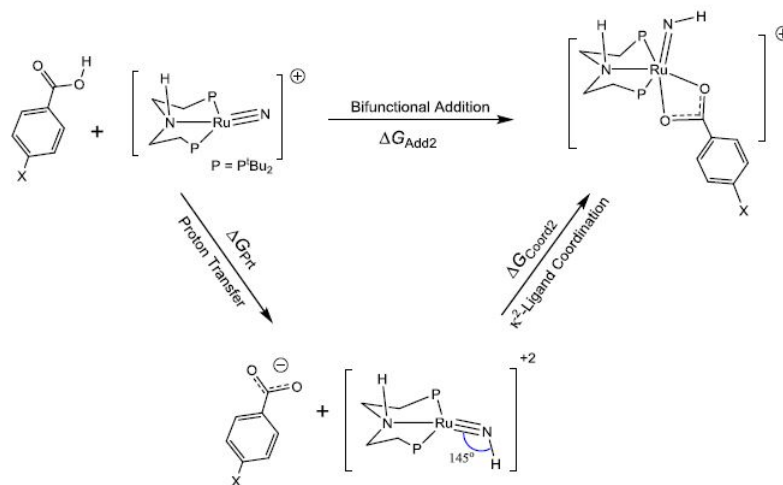
Figure 2.28: A devised reaction cycle representing the reaction between the acids and **2** giving the κ^2-intermediate **i2**.

Figure 2.22, which shows the full PES of the reaction between the substituted acids and **2** shows that both **i1** and **i2** have comparable energies (5.8 and 5.9 Kcal/mol respectively) this is in line with the data of the column graphs. The isomerization of intermediate **i1** to **i2** is known to pass through a low energy barrier [22], which in turn could reflect the small difference in thermodynamics between the steps.

The remainder of the mechanism exhibits approximately no difference in energy due to changing the acid, which is line with the prediction made earlier. The impact of changing the acid is felt up to formation of the **i2** intermediate and vanishes afterwards since the reaction center no longer involves any interaction of the acid moiety.
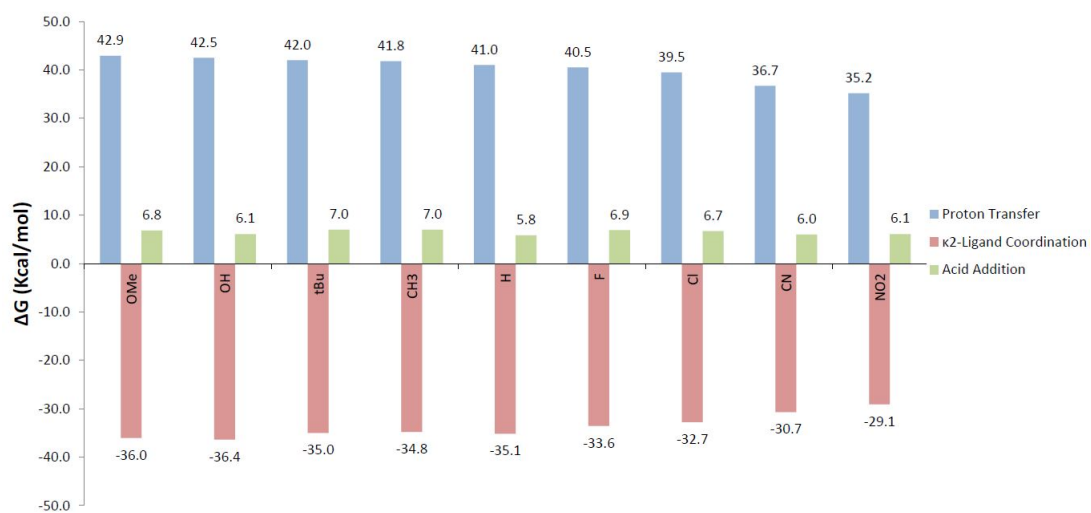
Figure 2.29: Column graph representing the energy steps for the κ^2-coordination cycle.

2.6.2 Effect of Varying the Metal Center

The first step in the mechanism proposed in Figure 2.8 is the step that is expected to exhibit the largest dependence on the nature of the acid. The results in the preceding section show this dependence to be quite small. It then becomes of interest to determine the effects of the metal on the energy profile of the reaction. The metal is immediately involved in each of the elementary steps in the full transformation. It is however not trivial to guess how the metal may influence these steps. In this section we use the calculations to investigate this effect. We divide the section into two parts, first we examine the effect of changing ruthenium into osmium. In this substitution there is no change in the oxidation state of the metal so the net charge remains positive. In the second part we change the ruthenium into technetium. To keep the same electronic structure, the oxidation state of the technetium should be Tc(III), so the net charge on the starting four-coordinate complex has to be neutral. The results of changing Ru into Os are summarized in Figure 2.30.
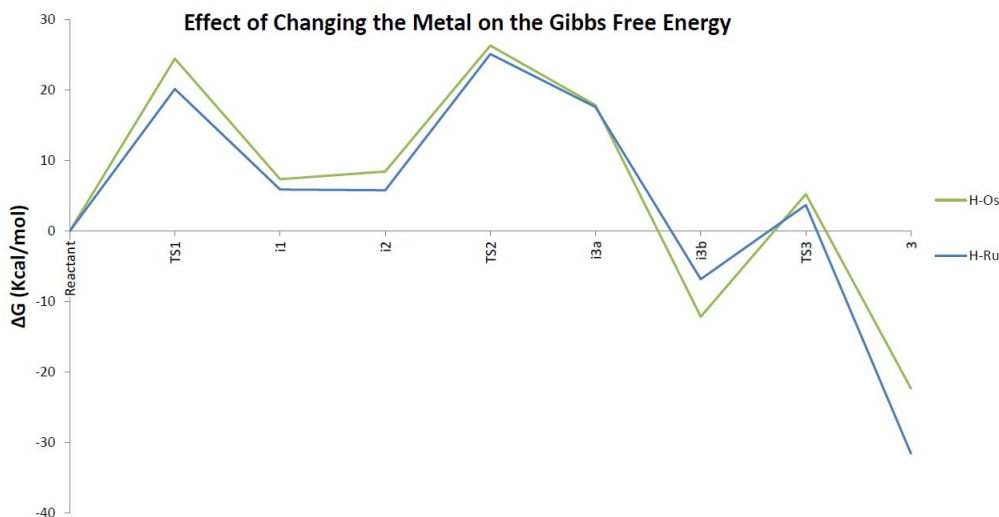
Figure 2.30: The full PES of the bifunctional reaction for Ru and Os.

Changing Ru(IV) to Os(IV) increases the barrier for the first bifunctional addition of benzoic acid across the MN bond by 2 kcal/mol: from 20.0 to 22.0 kcal/mol. Osmium substitution disfavors the thermodynamics of the addition reaction by 1.0 kcal/mol. Analysis of the given effect using the thermodynamic cycle shows, once more that the relatively small effect arises from cancellation of two opposing components. First proton transfer from carboxylic acid to the nitride is computed to be less favored by 3.4 kcal/mol in the osmium complex: $\Delta G_{Prt} = 41.0$ and 44.4 for Ru(IV) and Os(IV), respectively. This means the OsN bond is less basic than the RuN bond. It is hard to pinpoint the origin of the dif-
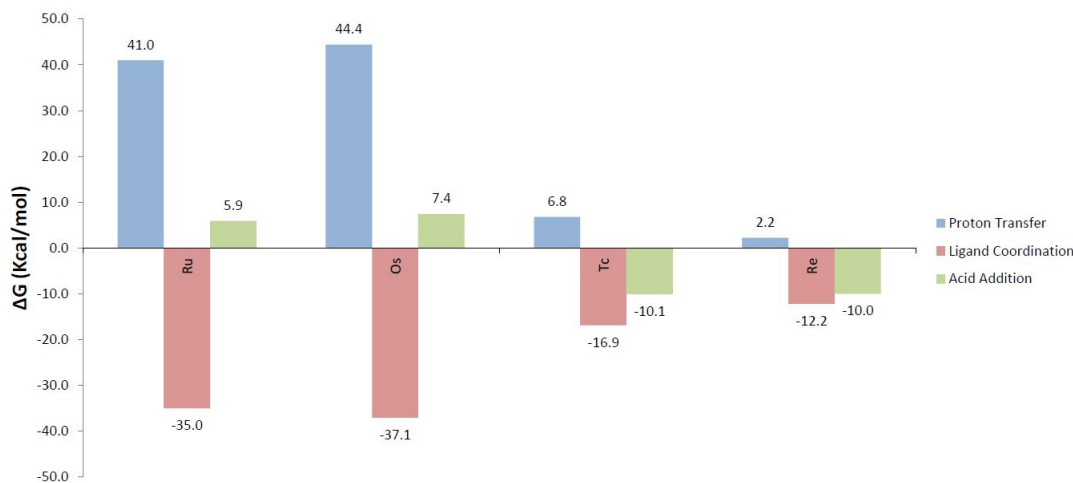
Figure 2.31: Thermodynamic cycle for the first step with different metal centers.

ference to one specific factor. Coordination of the benzoate anion to the M(NH) dication is more favored by 2.1 kcal/mol when M = Os compared to M = Ru: $\Delta G_{coord'n}$ = -35.1 and -37.1 kcal/mol for the ruthenium and osmium complexes, respectively. In general metal-ligand bonds are stronger for the third row transition metal complex than the second row ones. This effect is counterintuitive as the ions of the third row transition-metal elements have increased size that leads to longer M-L bonds and thus weaker bonds. The increase in strength is often attributed to relativistic effects that become more important in the heavier atoms.

Osmium substitution is computed to have little effect on the second protonation step leading to intermediate **i3a**. However, osmium substitution is computed to stabilize the rotated i3b by 3.5 kcal/mol relative to **i3a**, which is quite substantial.

The last PCET step in the proposed mechanism causes a changed in the oxidation state of the metal and is thus expected to be quite sensitive to the nature of the metal. Indeed, osmium substitution is computed to have a large unfavorable effect on both the kinetics and thermodynamics of the given step. Specifically: **i3b** encounters increased barrier for the PCET step 5.3 kcal/mol compared to 3.7 kcal/mol for the Ru-complex. Likewise, osmium substitution is computed to greatly disfavor the thermodynamics of the PCET step. The computed ΔG_{PCET} for the Ru and Os complexes relative to **i3b** are -24.7 and -10.7 kcal/mol, respectively. One way to account for the computed effects of osmium substitution on PCET is in terms of the loss of a bond in the process. As mentioned above, the individual M-L bonds are typically stronger for third row transition metals. In **i3b** there is one π-bond that is delocalized over the two amides making the N-Ru-N and N-Os-N moieties. This bond appears to be stronger with osmium. Upon PCET, this bond is lost, so PCET should be disfavored.

39

The overall reaction energy profile indicates that **TS2** remains the highest energy point on the reaction Gibbs free energy profile. The energy of this point is only 1.2 kcal/mol higher than the highest energy point on the energy profile of the ruthenium complex. However, osmium substitution is predicted to disfavor the net thermodynamics by 9.2 kcal/mol. Despite of this, the net thermodynamics of the transformation of the osmium complex remains quite exergonic: -22.3 kcal/mol. The calculations predict therefore that the given benzoic acid induced transformation should be both feasible both kinetically and thermodynamically.

To investigate the effect of the metal on the given reaction further, we also calculated the effect of substituting the Ru(IV) metal with Tc(III) on the full energy profile from metal nitride to the metal-ammine. The substitution keeps the d^4-electron count, but they lead to net neutral complexes. As would be expected based on the charge alone, the kinetics and thermodynamics of the first carboxylic acid bifunctional addition step are greatly stabilized in the neutral technetium complex, with the barrier being only 5.3 kcal/mol, and the thermodynamics is now exoergic by 10.0 kcal/mol. The results of changing Ru into Tc and Re are summarized in Figure 2.32.
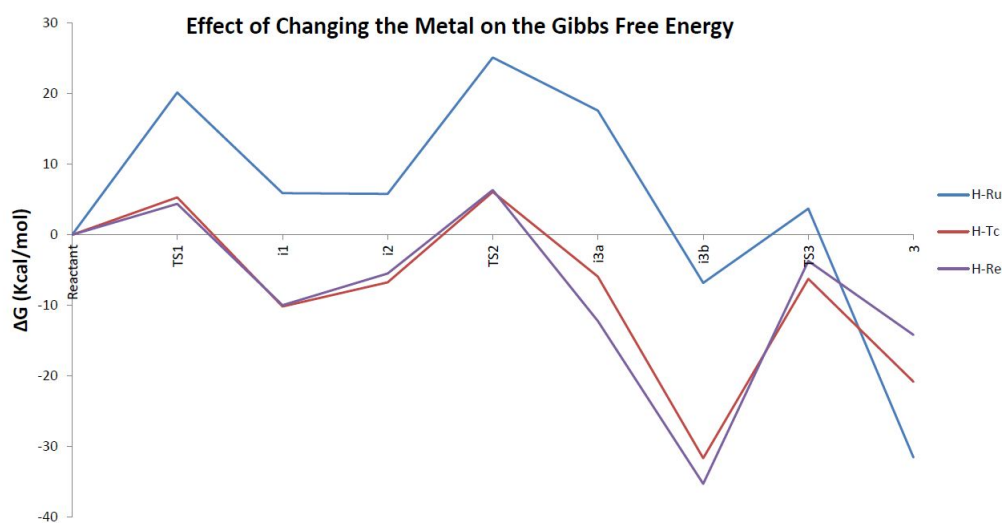
Figure 2.32: The full PES of the bifunctional reaction for Ru, Tc and Re.

The favorable thermodynamics of the given bifunctional addition was analyzed using the thermodynamic cycle. The results are summarized in Figure 2.31. The analysis reveals the proton transfer step to be rather low: $\Delta G_{Prt} = 6.8$ kcal/mol. The subsequent step of benzoate coordination is $\Delta G_{coord'n}$ in this case is -16.9 and thus drives the formation of the **i1** intermediate.

From i1, the energy input to reach the second proton transfer **TS2** is 16.2 kcal/mol. Intermediate **i3b** on the energy profile is -31.7 kcal/mol. Remarkably, the PCET originating from i3b is highly endorgenic in the Tc(III) reaction: + 11 kcal/mol. This is totally opposite to the Ru(IV) case. The result can be attributed to the nature of the oxidation states in the two complexes. The PCET step for Ru(IV) yields an ammine product with the ruthenium in the Ru(II) oxidation state. In contrast, the PCET reaction of the Tc(III) yields an ammine complex with technetium in the Tc(I) oxidation state, which is rather rare. Thus, according to the calculations, the neutral four-coordinate PNP-TcN complex should react rapidly with benzoic acid, but the reaction will stop at the Tc-diamido intermediate **i3b**. Technetium is rare chemical element. Calculations on the reaction between benzoic acid and the neutral Rhenium(III) complex leads to a similar conclusion.

Chapter 3

Search for a New Reaction: Bifunctional Acid Addition Induced Hydrogen Atom Transfer

3.1 Introduction

The initial calculations on the transformation of the RuN bond into Ru-NH$_3$ given in Figure 3.1 were conducted after the reaction was observed experimentally. To account for the transformation, the initial calculations proposed two unprecedented components, a concerted bifunctional addition of an acid like benzoic acid, and a concerted proton coupled electron transfer. The computed DFT energies indicated strongly that the proposed mechanism is energetically feasible. The mechanism could explain all the observation associated with the transformation.
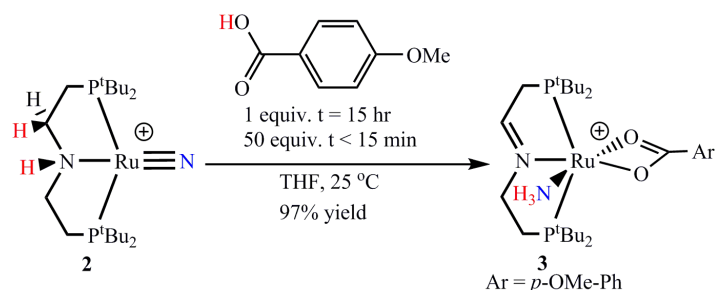
Figure 3.1: The formation of a metal ammine product by the new reaction between 4-methoxybenzoic acid and **2**.

The new study described in the previous chapter extended the use of the calculations to better understand the proposed mechanism. In particular, the calculations provided systematic new data on the effects of the acid and the metal on the elementary steps. These calculations provide important insight on the nature of the electronic structure requirements of the reaction. In light of the above studies, it becomes a challenge to be able to use the calculations to discover new reactions inspired from the elementary steps elucidated above. In this chapter we explore such possibility.

3.2   Idea for a New Reaction

According to the proposed mechanism, the key to the transformation in Figure 3.1 is the bifunctional addition reaction. In this reaction the unfavorable protonation of the nitride is assisted by coordination of one of the benzoate oxygens to the metal along with creation of an intramolecular hydrogen bond via a pericyclic six membered ring. The computed barrier for this step is near 20 kcal/mol, so it is chemically accessible. The subsequent intramolecular proton transfer has a similar energy as the first bifunctional addition step.

The bifunctional addition step generates intermediate **i1** with a metal imine bond Ru=NH. Obviously, the Ru=NH group is expected to be more reactive than the RuN bond. As such, in searching for a new reaction mode, we reasoned the bifuctional addition step may induce new reactions that are more relevant to M=NH chemistry. For the purpose of the present study we are interested particularly in completing the transformation of the RuN bond into Ru-NH$_3$. In this chapter we use the calculations to explore if a benzoic acid induced Ru-ammine product can be formed by an intermolecular reaction with a hydrogen atom donor. If the energetics are right, this will provide a fundamentally different reaction mode from the observed intramolecular proton coupled electron transfer. We chose to work with the hydrogen atom donor (2,2,6,6-Tetramethylpiperidin-1-yl)oxyl, commonly known as TEMPOH as the hydrogen atom donor. TEMPOH has been chosen due to its low bond dissociation energy (BDE) of the O-H which is experimentally determined to be 70 Kcal/mol (30% less than that of a normal O-H bond). As such TEMPOH is used as a source of H-atom (distinguishing it from the proton transfer of the traditional mechanism). The stability of the radicals formed when using TEMPOH is enhanced by the delocalization of the electron on a 2-center-3 electron N-O bond.

3.3 Reaction of 2 with benzoic acid and two equivalents of TEMPOH.

We begin our investigation by comparing the relative reaction energies for the individual reactions of benzoic acid addition to **2**, and the energy for hydrogen atom transfer from TEMPOH to **2** (Figure 3.2).
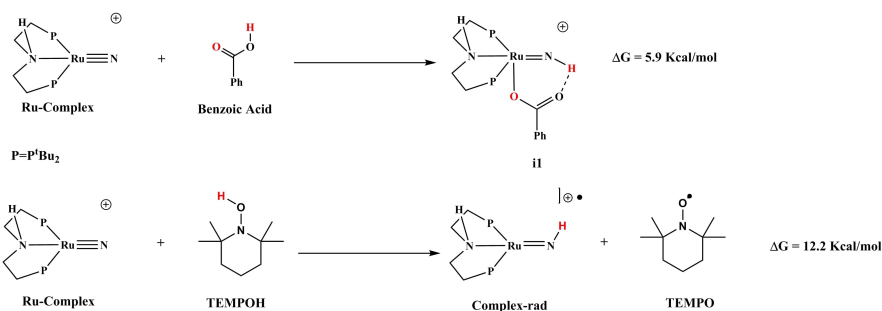
Figure 3.2: The relative reaction energies for the reaction between **2** and benzoic acid or TEMPOH.

The calculations predict both reactions to be endergonic. However, the reaction energy of benzoic acid is only 5.9 kcal/mol. In contrast, the reaction energy of hydrogen atom transfer is 12.2 kcal/mol. This means if a mixture of benzoic acid and TEMPOH is added to **2**, the primary reaction will be between **2** and benzoic acid.

We now proceed with the reaction between intermediate **i1** and TEMPOH. The results are given in Figure 3.3. The optimized product from the first hydrogen atom transfer in Figure 3.3 is intermediate **i2'**. This is a ruthenium-amide cation radical with κ^1-coordination of the benzoate group. Interestingly, in **i2'** the initial hydrogen bond characteristic of **i1** is lost. In **i2'** the new NH_2 moiety is near planar and is nearly coplanar with the P-Ru-P plane. Despite the loss of the hydrogen bond, the calculations predict the Gibbs free energy of H-atom transfer leading to **i2'** to be exergonic (-11.2 kcal/mol).

Our search for a transition state for the given reaction identified **TS2'**. The O-H donor bond in **TS2'** is stretched only slightly to 1.16Å, and the N-H bond in the making is quite long (1.35Å). The initial H-bond is lost in this **TS2'** and the computed activation free energy defined from the separated i1 and TEMPOH to **TS2'** is 22.0 kcal/mol. Next, we calculated the octahedral κ^2-complex of the radical cation, namely **i3'** in Figure 3.3. Surprisingly, the κ^2-complex is computed to be 4.1 kcal/mol above the κ^1-intermediate **i2'**. Apparently, the Ru=NH_2 π-interactions in the κ^1-intermediate **i2'** are highly favorable.
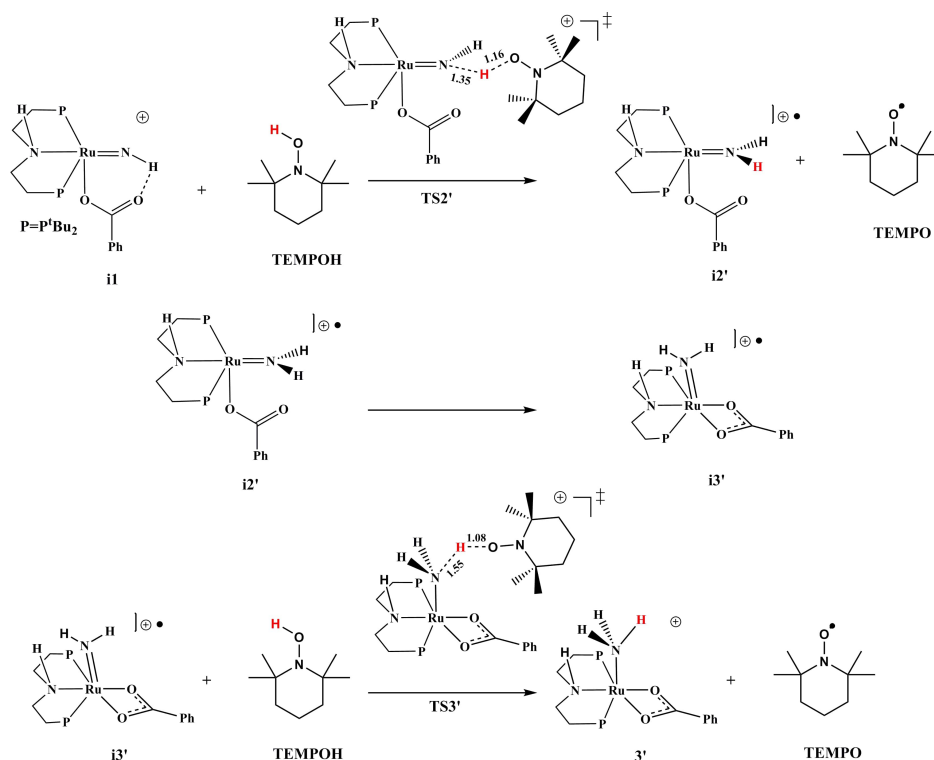
Figure 3.3: A scheme depicting the reaction between **i1** and two equivalents of TEMPOH

From **i3'** we calculated the reaction of with another TEMPOH to afford the final Ru-ammine product of interest **3'**. This reaction is highly exergonic: -11.2 kcal/mol, relative to the separated **i3'** and TEMPOH. We identify a transition state for this step **TS3'** characterized by a short O-H bond and a long N-H bond distances, 1.08 and 1.55Å, respectively. These parameters implicate an early, reactant like transitions state. Consistently, the barrier for this step relative to the separated **i3'** and TEMPOH is 16.5 kcal/mol, much lower than the barrier of the first reaction.

The highest energy point on the free energy profile of the reaction of **2** with benzoic acid and two TEMPOH molecules is 27.9 kcal/mol, for the transition state of first HAT step (**TS2'**). This energy is much higher than the highest energy point on the intramolecular PCET. The given profile assumes the first HAT takes place on the initial κ^1-benzoate Ru=NH intermediate **i1**. As an alternative we calculated the possibility of initial isomerization of **i1** to the corresponding κ^2-benzoate Ru=NH intermediate **i2**. Gratifyingly, we find the HAT barrier of this isomer taking place by transition state **TS2"** to be 20.2 kcal/mol, much lower than the corresponding one via **TS2'**.
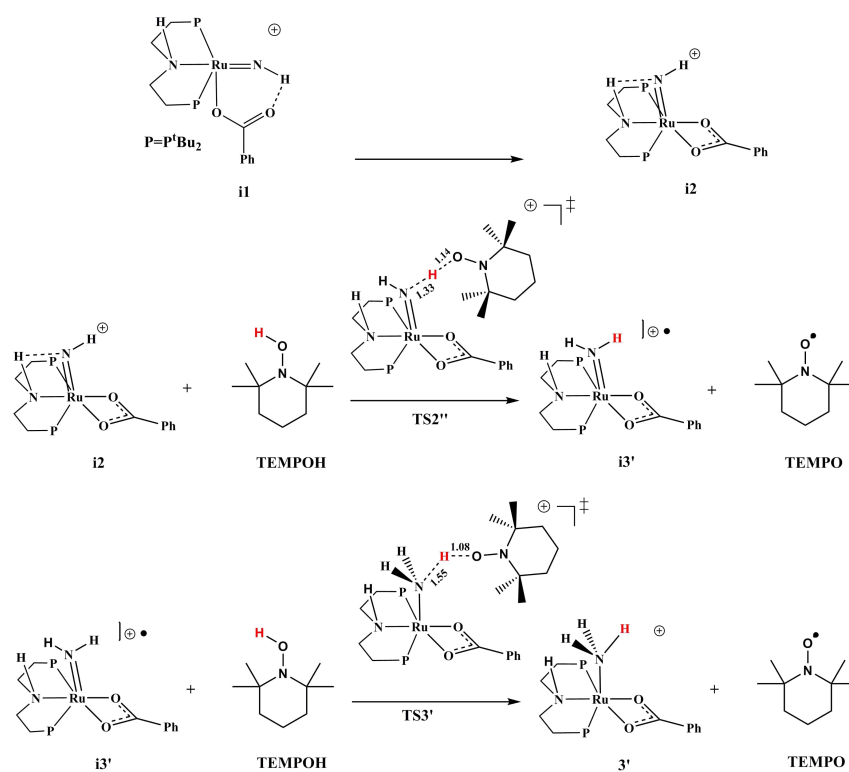
Figure 3.4: A varaiation on the reaction scheme in Figure 3.3, showing the intermolecular reaction with two equivalents of TEMPOH at different steps in the mechanism.

The full computed energy profile for the reaction on 2 with benzoic acid and two equivalents TEMPOH is shown in Figure 3.5. The net transformation is highly exergonic: -18.3 kcal/mol. This means there is a very large driving force for the reaction. Figure 3.5 shows **TS1** for the bifunctional addition of benzoic acid and **TS2"** for the first HAT to have similar energies 20.2 kcal/mol. This means the given new transformation should be kinetically accessible at room temperatures.
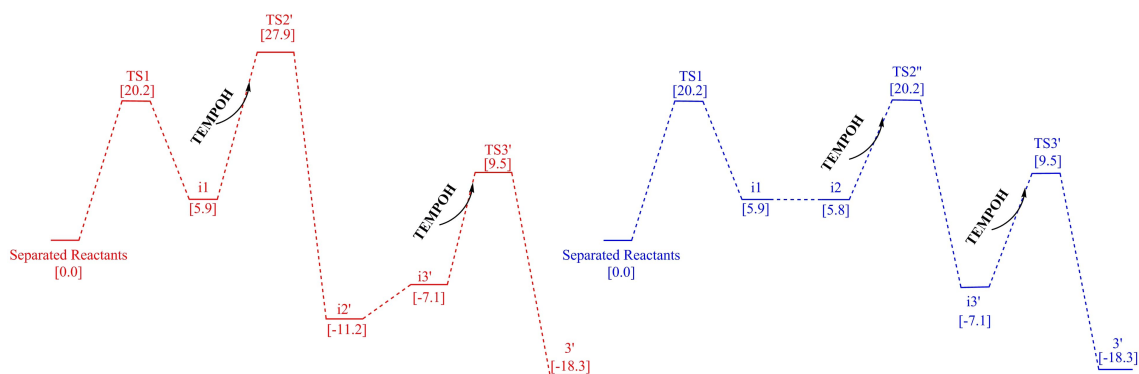
Figure 3.5: The full PES for the reaction with two equivalents of TEMPOH. The difference between the red and blue plots refers to different computed reaction pathways.

3.4 Reaction of 2 with benzoic acid and one equivalent TEMPOH.

The κ^2-benzoate Ru=NH$_2$ free radical cation intermediate **i3'** that is formed following **TS2"** in the reaction of the first TEMPOH with **i2** can in principle undergo an intramolecular proton transfer reaction from the NH center of the PNP ligand to the nitrogen on the Ru=NH$_2$ group (Figure 3.6). A second TEMPOH can in turn transfer a hydrogen to the deprotonated PNP ligand. This can therefore provide an alternative route to the Ru-NH$_3$ product **3'**. We became interested to know the energy profile of this step. The results are summarized in the green plot of Figure 3.5.
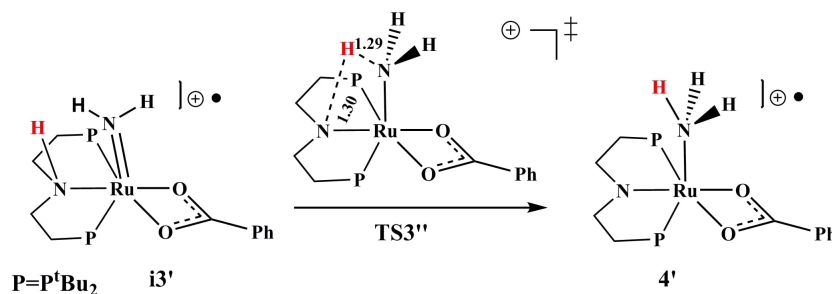
Figure 3.6: The intramolecular step of the proton transfer from the pincer nitrogen.

Remarkably, the intramolecular proton transfer step within the free radical cation intermediate **i3'** to give the ammine radical cation **4'** is computed to be exergonic by a full 14 kcal/mol and the barrier of the reaction is only 14.7 kcal/mol (both energies relative to **i3'**). The energy of **4'** relative to the separated reactants is -21.0 kcal/mol (Figure 3.7). This means that **2** is likely to react with only one equivalent of TEMPO to produce the unsaturated octahedral Ru-NH$_3$ radical cation as an observable final product.
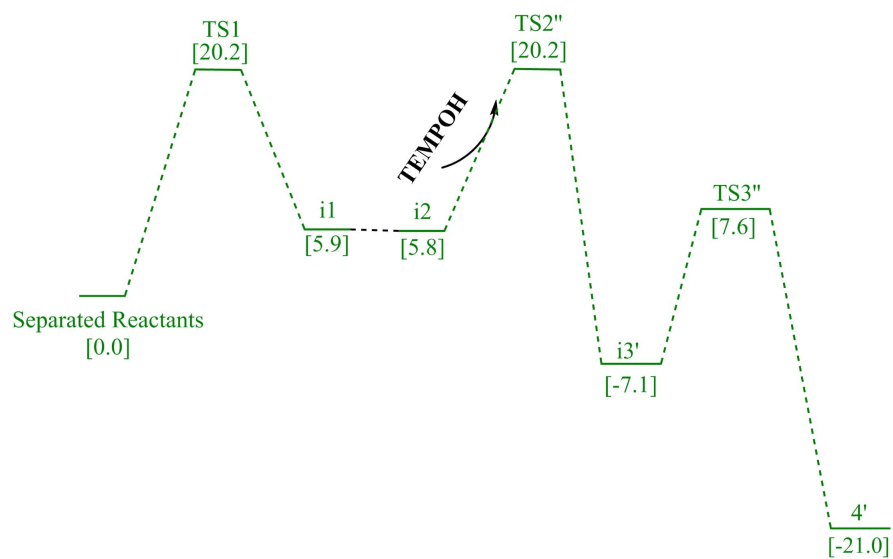
Figure 3.7: The PES for the intramolecular step of the proton transfer from the pincer nitrogen.

3.5   Recommended Experimental Studies

In light of the results above we can suggest two experiments that will demonstrate new modes of new reactions triggered by benzoic acid addition to the four coordinate ruthenium nitride complex **2**. The first involves reaction with one equivalent benzoic acid and one equivalent TEMPOH. The second is involves reaction with one equivalent benzoic acid and two equivalents TEMPOH. To avoid complications with the intramolecular proton transfer, we recommend the use of a PNP complex that lacks a hydrogen on the pincer nitrogen **1** (Figure 3.8). The (PNP)RuN complex build on the pyridyl PNP ligand will probably be an ideal candidate for this purpose.
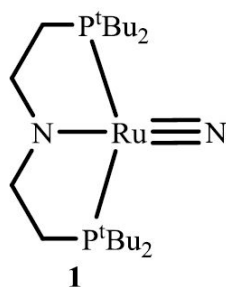
Figure 3.8: (PNP)Ru Complex **1** lacking the hydrogen on the pincer nitrogen.

Chapter 4

Mechanism and Products of Decomposition of an Octahedral Iridium Alkoxide Complex

4.1 Ester Formation by Dehydrogenative Coupling

Esters are among the most encountered molecules in everyday life, being present in both nature and industry. The versatility of esters is apparent by their presence in many industrial fields such as food, perfumes, soaps, and plastics. For instance, the odor of common fruits is the result of the presence of simple esters (Figure 4.1).
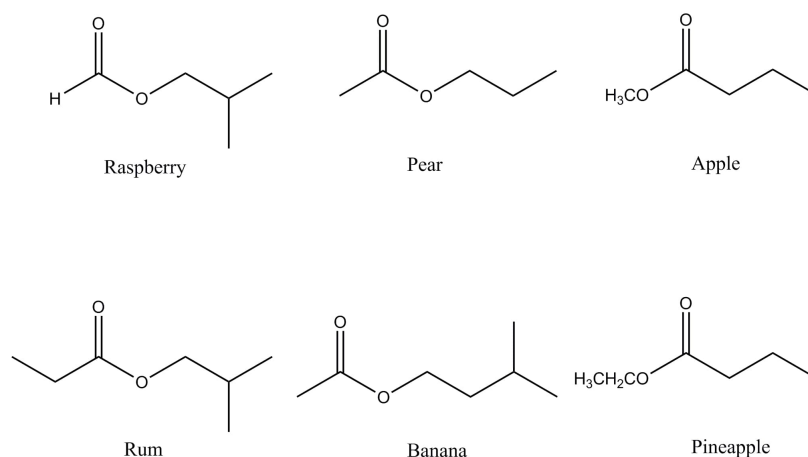
Figure 4.1: Various natural esters and their associated fruit odor.

In industry, esters are commonly used in their polymer form (polyesters) in fabric, acrylate esters in plastics and cellulose acetate esters in photography (Figure 4.2).

Poly(methyl acrylate)

Cellulose acetate
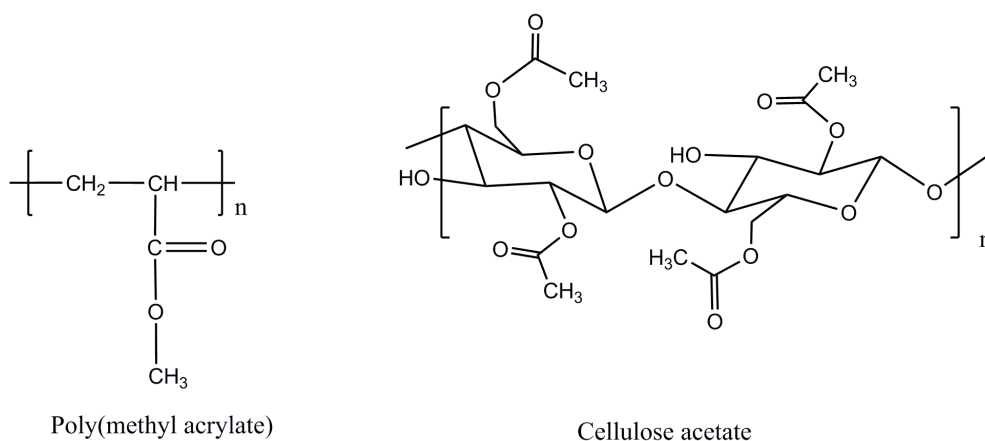
Figure 4.2: Various synthetic esters used in different industries.

There are numerous methods for the preparation of esters, such as the carbonylation of alkenes, and the Tishchenko reaction where in the presence of an alkoxide and an aluminum catalyst, aldehydes undergo disproportionation. Of importance and a primary method for preparing esters is the Fischer esterification, where a carboxylic acid is treated with an alcohol in the presence of an acid as a catalyst to give the corresponding ester (Figure 4.3). The reaction is reversible and thus can be manipulated using Le Chatelier's principle to drive the reaction towards ester formation.

Carboxylic Acid   Alcohol   Ester   Water
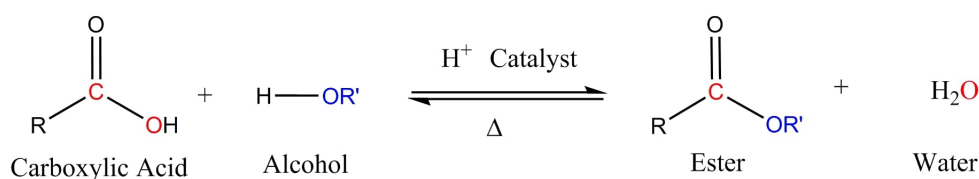
Figure 4.3: General reaction for the preparation of esters using the Fischer esterification.

Fischer esterification depends on a strong acid, such as H_2SO_4, to catalyze ester production. In an industrial setting, this reaction is fundamental for the organic synthesis of many esters, therefore, the large use of strong acids and activators is a negative consequence of such synthesis. This sparked the interest of chemists to develop atom-efficient, environmentally friendly alternative routes for the production of esters. Particularly, the acceptor-less dehydrogenative coupling of alcohols

into esters, resulting in the release of hydrogen gas seems to be a plausible alternative route. Dehydrogenative coupling is an atom efficient method that is important from a fundamental perspective and can be used to mass produce H_2 biofuel. Furthermore the green attributes of this synthetic route is the possibility of ester hydrogenation.

In 1981, Murahashi reported the oxidative condensation of alcohols into their esters using a ruthenium catalyst (Figure 4.4)[29]. The reaction is described as a simple and highly efficient along with the possibility of facile isolation of the product. The proposed mechanism for this reaction begins with the oxidative addition of dihydridotetrakis(triphenylphosphine)-ruthenium to the OH bond of a primary alcohol, followed by the β-elimination giving a aldehyde and a ruthenium dihydride complex. A hemiacetal is formed by the reaction of a the aldehyde and the alcohol, which then undergoes another dehydrogenative step giving the ester and hydrogen gas. This work marked the beginning of an ever evolving field of homogeneous catalysis for the purpose of synthesising esters.

$$2\ RCH_2OH \xrightleftharpoons{RuH_2(PPh_3)_4} RCO_2CH_2R\quad +\quad 2H_2$$
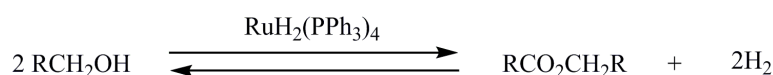
Figure 4.4: Oxidative condensation of alcohols using a ruthenium complex.

4.2 Possibility for an Outer Sphere Dehydrogenative Coupling Mechanism

Insertion of unsaturated substrates like olefins and ketones into a metal-hydride bond and its reverse de-insertion are among the most fundamental reactions in transition metal chemistry, and are widely implicated in catalysis. As illustrated for a ketone in Figure 4.5, insertion typically proceeds by binding of the substrate into the inner coordination sphere of the metal at a site cis to the hydride to allow hydride transfer and to the carbonyl and metal-alkoxide bond formation. According to this general mechanism, insertion of an unsaturated substrate into a coordinatively saturated metal-hydride complex would require initial substitution of one of the ligands by the unsaturated substrate.

In 2002, Morris and coworkers synthesized the trans-dihydride BINAP diamine complex (**4-H** in Figure 4.6) and showed it is an efficient catalyst for the hydrogenation of unactivated ketones [30]. To our knowledge, **4-H** was the first example of a ketone hydrogenation catalyst that did not require initiation by
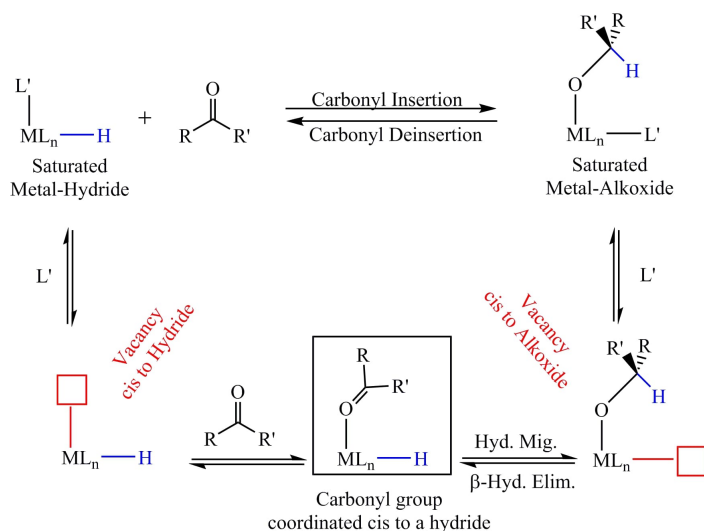
Figure 4.5: Conventional inner-sphere carbonyl group insertion/de-insertion.

alkali-alkoxide base, and the first unambiguous example of an octahedral d^6-trans-dihydride complex to be used in hydrogenation catalysis. Morris and coworkers proposed catalysis by **4-H** to follow an outer-sphere bifunctional Noyori-type mechanism involving formation and reaction of an unsaturated amido intermediate.
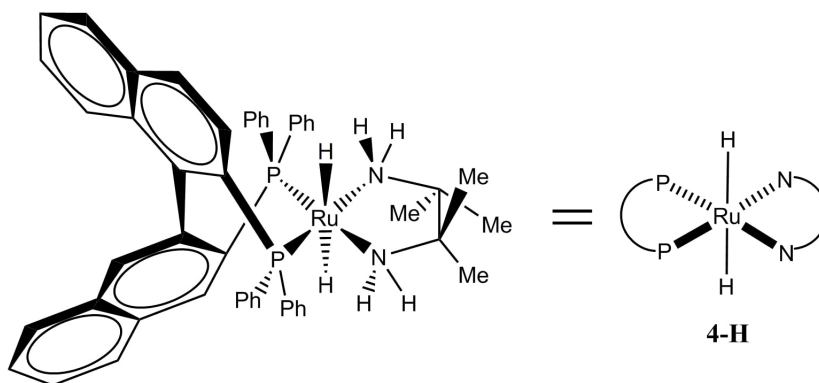
Figure 4.6: Trans-dihydride BINAP diamine complex **4-H**.

In 2005, Bergens and coworkers observed that addition of one equivalent of acetophenone to a solution of **4-H** in THF at low temperature leads to rapid and quantitative carbonyl group insertion producing an octahedral d^6-trans-hydrido-alkoxide (**4-OCHMePh** Figure 4.7) [31].

Bergens argued that the bidentate ligands in **4-H** would rule out the possibil-
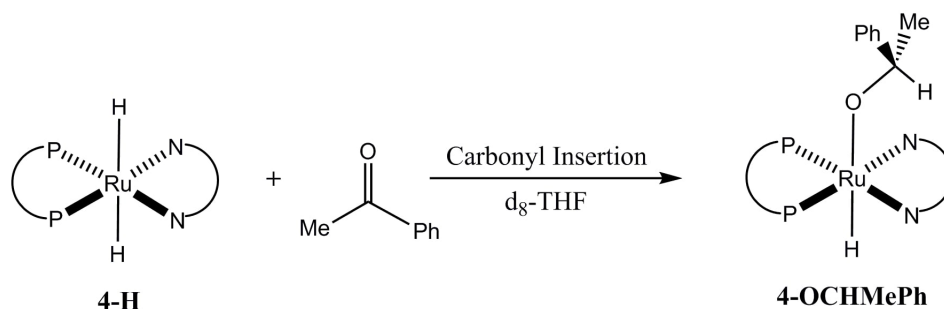
Figure 4.7: Insertion of a carbonyl group into the trans-dihydride BINAP diamine complex giving an octahedral d^6-trans-hydrido-alkoxide **4-OCHMePh**.

ity of a conventional inner-sphere insertion pathway, and this proposition was supported by novel mechanistic experiments. The insertion in Figure 4.7 was surprising because according to the accepted bifunctional Noyori mechanism the reaction should give an alcohol and an unsaturated amido complex as kinetic products.

In 2006 Milstein and coworkers reported the unsaturated de-aromatized square pyramidal PNN-pincer complex **5** (Figure 4.8) to catalyze dehydrogenative coupling of two primary alcohols into an ester with the release of two H_2 molecules [32]. This and related reactions catalyzed by **5** are of great interest in green synthesis and have potential for large scale applications, like biomass production of H_2.
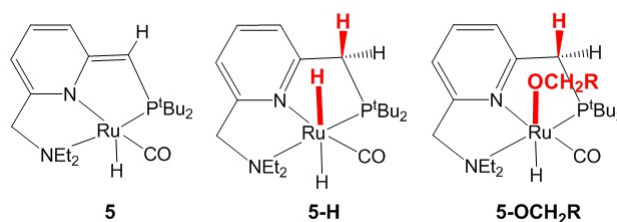
Figure 4.8: Milstein's catalyst and the octahedral hydride and the alkoxide products form heterolytic H_2 and RCH_2OH addition.

The de-aromatized complex **5** is known to undergo heterolytic metal-ligand cooperative (MLC) addition of H_2 and primary alcohol yielding the octahedral trans-dihydride and trans-hydrido-alkoxide octahedral products **5-H** and **5-OCH_2R**, respectively (Figure 4.8). Thus to account for catalysis using **5**, Milstein proposed a Noyori-type mechanism as outlined in Figure 4.9.

First an alcohol is dehydrogenated by **5** via an MLC mode to give an aldehyde.
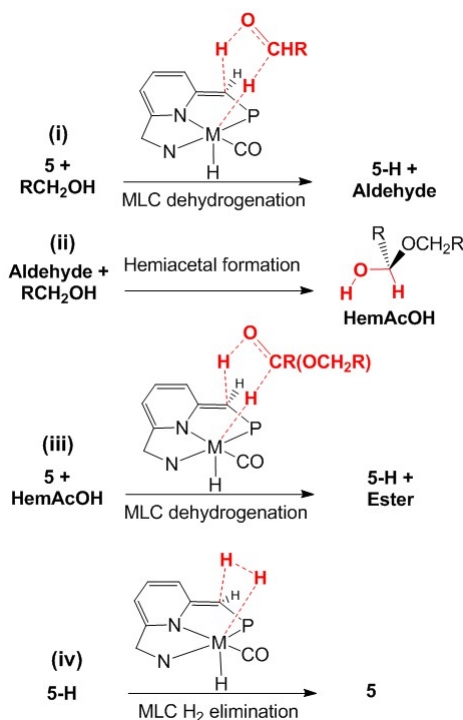
Figure 4.9: A Metal-Ligand Cooperative Mechanism for dehydrogenative coupling of alcohols into esters catalyzed by **5**.

The aldehyde was then proposed to react with another alcohol to give a hemiacetal. This step can proceed without a catalyst. The hemiacetal is an alkoxy substituted alcohol, so the MLC mechanism invokes a role for another unsaturated **5** to dehydrogenate the hemiacetal and produce the final ester (step iii in Figure 4.9). According to this mechanism the catalyst is regenerated by an MLC loss of H_2 from the octahedral dihydride product from the two MLC dehydrogenation steps. The MLC mechanism was the subject of several theoretical studies.

In a series of theoretical studies conducted at AUB, Hasanayn and coworkers proposed an alternative to the MLC mechanism as outlined in Figure 4.10 [33, 34, 35]. Given that **5** readily reacts with alcohols, Figure 4.10 takes the saturated octahedral ruthenium alkoxide **5-OCH₂R** as the starting point in dehydrogenative coupling. The calculations identified a transition state for an unconventional aldehyde elimination from **5-OCH₂R** to produce an aldehyde and the octahedral **5-H**. The calculations provided evidence that the aldehyde produced in the latter step can react directly with a second **5-OCH₂R** to give a hemiacetaloxide ion-pair that rearranges to give the final ester and another dihydride complex **5-H**. The net transformation from the aldehyde and **5-OCH₂R** to the ester and **5-H** was proposed to be best viewed as an unconventional organometallic

57

H/OCH_2R metathesis in which a hydride and an alkoxide are switched between a metal and an acyl group.
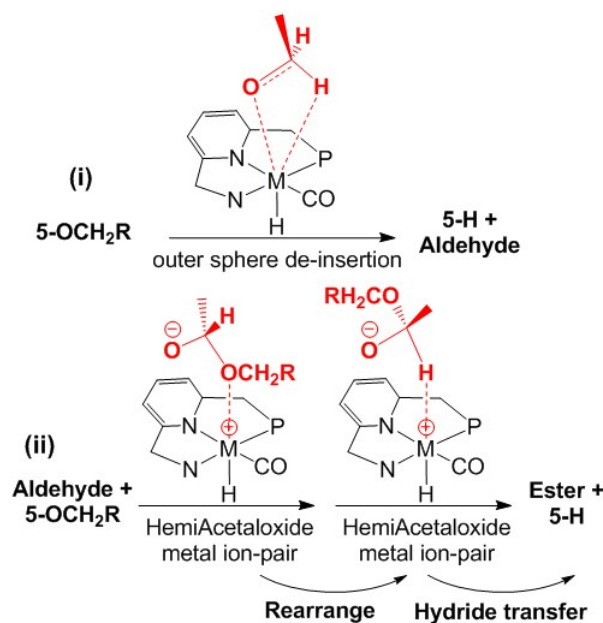
Figure 4.10: Alcohol based mechanism for dehydrogenative coupling of alcohols into esters.

Comparing both reaction mechanisms, we note that the MLC revolves around the de-aromatized form of the catalyst, while the alcohol based mechanism suggests a mechanism revolving around the metal-alkoxide species. In fact, the de-aromatized form of the catalyst is also the alkoxide species (Figure 4.11, as such postulating the alcohol based mechanism is supported by the results of the studies done on the Milstein catalyst.
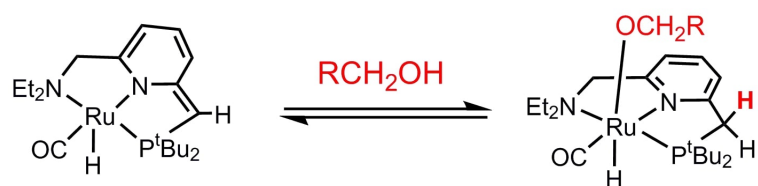
Figure 4.11: The de-aromatized form of the catalyst after the formation of the alkoxide species.

DFT supports the plausibility of a mechanism that revolves around the metal-alkoxide species. If we look at the computed molecular geometry (Figure 4.12) of the Milstein catalyst, we observe a long and tilted Ru-OR bond suggesting that the bond nature to be weak and most likely has a dominant ion-pair character. This motivated the Hasanayn group to investigate aldehyde formation by slippage of the alkoxide that brings a C-H bond over the metal.
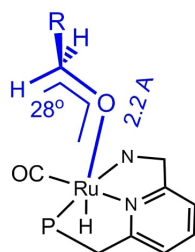
Figure 4.12: Computed geometry for the alkoxide de-aromatized geometry of the Milstein catalyst.

As such a different mechanism for the dehydrogenative coupling by a metal-alkoxide was proposed, showing the de-insertion of an aldehyde by an outer-sphere reaction mode. The net reaction in such a reaction can be considered a non-classical β-elimination taking place without the presence of a cis-vacant site. The full reaction mode for the Milstein catalyst is show in details in Figure 4.13.
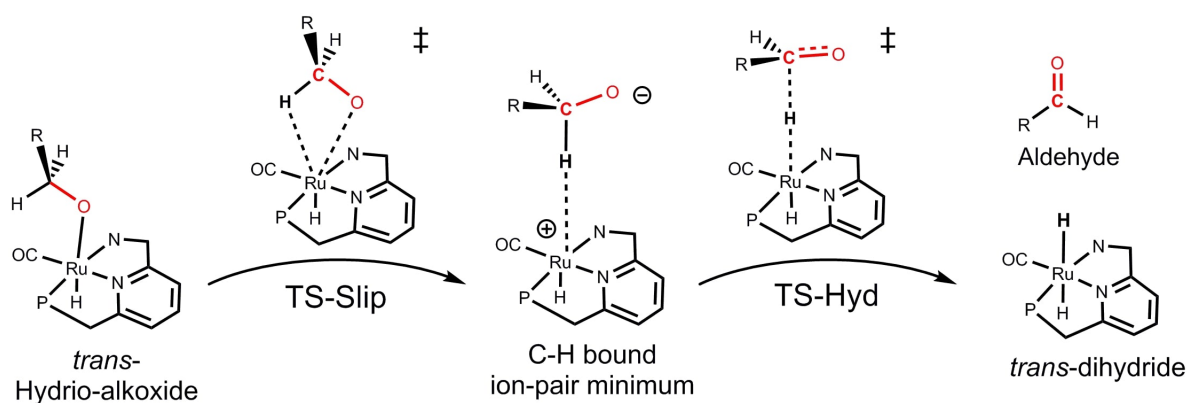
Figure 4.13: Computed geometry for the alkoxide de-aromatized geometry of the Milstein catalyst.

4.3 Milstein Complex: Case study for no cis-vacant site complexes

The MLC and alkoxide based mechanisms account for alcohol dehydrogenative coupling in fundamentally different ways. The computed energy profiles of the two mechanisms are comparable. Given the very different nature of the reactions on the two profiles, one may not rule out one mechanism or another. The two mechanisms have important implications to catalyst design. Specifically, the alkoxide-based mechanism implies some octahedral metal-alkoxide complexes that lack functionality necessary for MLC could in principle be able to undergo transformation into an ester and an octahedral metal-hydride. Herein we propose to use the calculations to identify such systems.

By reviewing the literature of octahedral metal-alkoxide complexes, to our surprise, we found a study, also by Milstein, reporting an octahedral iridium-alkoxide complex decomposing into a metal hydride and an aldehyde (Figure 4.14) [36]. Significantly the given study reports that aldehyde de-insertion to be catalyzed
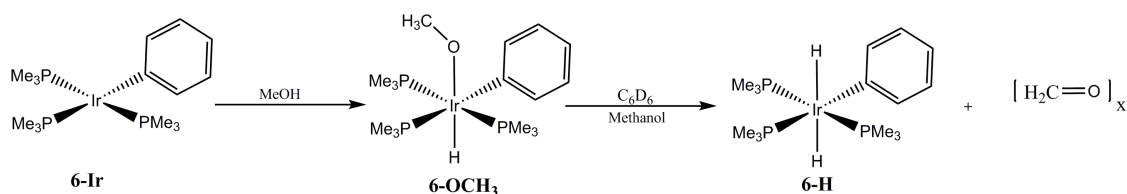
Figure 4.14: Decomposition of an iridium-alkoxide complex into a metal hydride and aldehyde.

by methanol. An elegant set of isotope labelling experiments provided strong evidence that the reaction does not follow the usual pathway requiring a vacant coordination site. Note such reaction was invoked computationally in Figure 4.10. Milstein speculated the reaction follows formation of a solvent separated methoxide ion-pair and C-H activation of one of the solvating methanol molecules. The study further stresses the formation of the trans-dihydride (**6-H**) and does not dwell sufficiently on the characterization of the other product and settles for reporting them as formaldehyde oligomers. To our knowledge this is the only unambiguous example of an aldehyde de-insertion taking place without a coordination site. We are not aware of any theoretical studies on the given aldehyde de-insertion reaction. We find this system can be very useful to support or refute some of the ideas proposed in Figure 4.10. We therefore propose to undergo a detailed systematic theoretical investigation on this system.

We started our investigation with calculation of the thermodynamics of aldehyde elimination from **6-OCH_3**. The results are summarized in Figure 4.15. Surpris-

ingly, the calculations predict aldehyde de-insertion to be uphill by at least 6.3 kcal/mol. Note that DFT methods are usually reliable when it comes to thermodynamics. The agreement among the different theoretical levels that de-insertion is unfavorable gives strong confidence in the calculated results. Interestingly, evidence for aldehyde production in the given system was made using a visual test, rather than being confirmed by a standard spectroscopic technique like NMR.

Complex	Benzene Continuum			Methanol Continuum
	M06L	M06	ωB97xd	M06L
6-OCH$_3$	8.9	7.3	6.3	10.9

Figure 4.15: Free energy of formaldehyde de-insertion from octahedral complex.

Noteworthy, Milstein made the point that the aldehyde is in fact formed in an oligomeric form ($[CH2O]_x$), but no details were given on how the oligomer was characterized. This means that the thermodynamics of the decomposition of **6-OCH$_3$** is driven by further reaction of formaldehyde. The mechanism of aldehyde oligomerization will require reaction of at least two aldehydes at some point. Given the computed uphill thermodynamics, the steady state concentration of the aldehyde from de-insertion from **6-OCH$_3$** will be too small for the kinetics of oligomerization to be chemically significant. As an alternative to oligomerization, and in light of the mechanism considered in Figure 4.10, we considered the possibility that a formaldehyde produced by de-insertion from **6-OCH$_3$** may be undergoing an H/OCH3 metathesis with another **6-OCH$_3$** molecule to produce **6-H** and methylformate. In sharp contrast with the energies in Figure 4.15, our calculations predict the thermodynamics of this reaction to be highly exergonic and at all theoretical levels (Figure 4.16). According to our preliminary results therefore, it is likely that decomposition of **6-OCH$_3$** to be thermodynamically driven by ester formation not aldehyde oligomerization.

Complex	Benzene Continuum			Methanol Continuum
	M06L	M06	ωB97xd	M06L
6-OCH$_3$	-15.0	-17.4	-19.2	-14.8

Figure 4.16: Free energy of ester formation from the reaction of octahedral complex with formaldehyde.

4.4 Computed Outer-Sphere PES for Formaldehyde Deinsertion

We have also conducted some calculations on the mechanism of aldehyde de-insertion from **6-OCH_3**. When the calculations are done in a benzene continuum, the barrier to de-insertion is calculated to proceed via a slippage transition state that rotates the methoxide into an ion-pair minimum in which the C-H bond of the methoxide is pointed to the metal, as described in Figure 4.10. The ion-pair then transfers a hydride to the metal and aldehyde de-insertion is completed. The highest energy point on the given stepwise sequence of reactions is for the rearrangement step (TS-Slip), at 27.1 kcal/mol. This is a quite high a barrier, which is consistent with the experimental observation that no decomposition of **6-OCH_3** is observed in the absence of methanol.
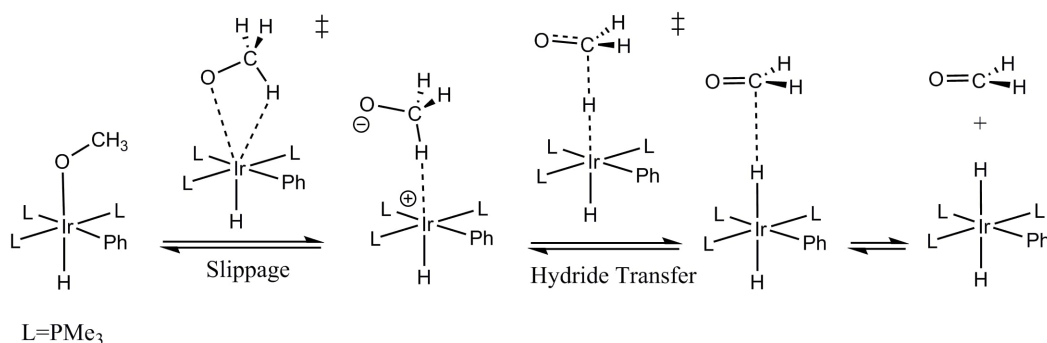
Figure 4.17: Illustration of the proposed dehydrogenative coupling mechanism facilitated by an H/OR metathesis mediated via an ion pair intermediate.

When the calculations are conducted in a methanol continuum we observe that the rearrangement step (TS-Slip) is lowered by 17.7 Kcal/mol (Figure 4.18), suggesting that methanol plays a key role in the decomposition of the **6-OCH_3** complex, which is in line with the experimental analysis proposed by Milstein.

The calculations where then conducted on the same system while utilizing explicit methanol solvent molecules (using one or two explicit molecules) in benzene continuum, mimicking the experimental conditions that Milstein used. The orientation of the solvent molecules can vary depending on the type of bonding occurring between the complex and the solvent. In order for us to show the catalytic effect of methanol in this system we sufficed by introducing solvent molecules as shown in Figure 4.19.

The computed energies clearly show the catalytic effect of methanol on the system. When no explicit methanol was used (only benzene continuum) the TS-Slip barrier was 27.1.0 Kcal/mol. Upon addition of the first methanol molecule, the barrier drops by 2.0 Kcal/mol. The effect is further increased by the addition of another solvent molecule, giving a barrier of 22.0 Kcal (another decrease by
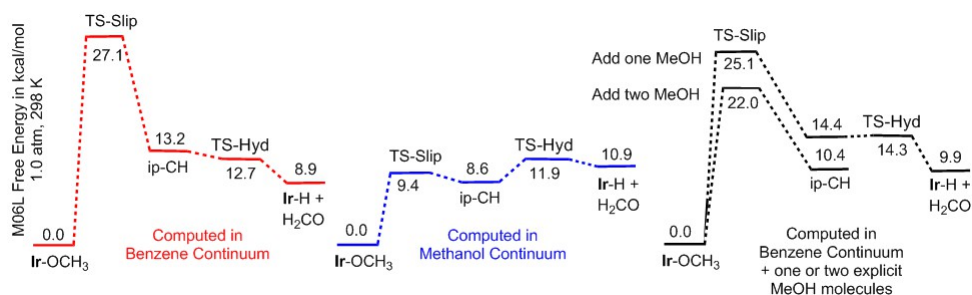
Figure 4.18: Energy profiles depicting the steps of formaldehyde de-insertion from the **6-OCH₃** complex in benzene and methanol continuum. A third energy profile shows the use of explicit methanol solvent molecules in benzene continuum.
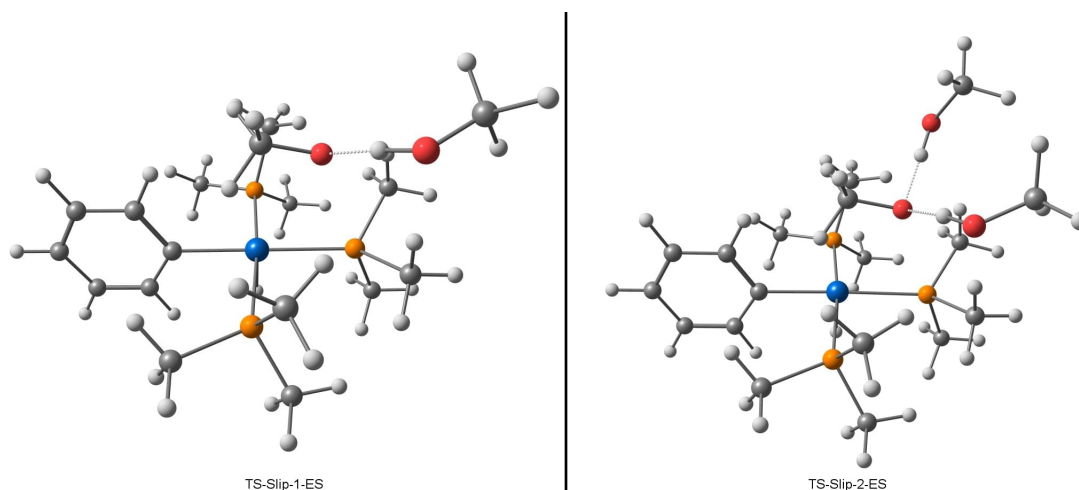
Figure 4.19: The geometries of the TS-Slip computed with either one (1ES) or two (2ES) solvent molecules.

3.0 Kcal/mol). These observations are in line with the experimental observations made my Milstein. Further more it is interesting to note that upon addition of each methanol solvent the barrier dropped by approximately 2 - 3 Kcal/mol. While further addition of solvent molecules can only be done using a different type of computational techniques (dynamic modeling), we are able to conclude the ability of our calculations to reproduce an experimental observation, further increasing their credibility of the system under study.

Based on the previous calculations, be it in benzene, methanol or using explicit methanol solvent molecules we showed that the de-insertion of the aldehyde is thermodynamically unfavorable. We previously showed that the formation of the ester in this system is more favorable and thus we proceed to compute the complete mechanism and PES for formation of the ester from the reaction between **6-OCH₃** and a formaldehyde molecule formed in Figure 4.17.

4.5 Ester Formation: Favorable Thermodynamic Products

The reaction is initiated by the reaction between **6-OCH₃** and one molecule of formaldehyde through a low energy migration step (typically proceeding through precomplex formation between the iridium alkoxide and the formaldehyde). The result of this migration step is the formation of an ion pair with the oxygen of the newly formed hemiacetaloxide pointing towards the metal. As with the previous mechanistic description, the next step will be a rearrangement step occurring through another TS-Slip yielding the other ion pair with the hydrogen pointing towards the metal. Finally a hydride transfer step occurs, yielding a transhydride complex along with methylformate (an ester). The complete mechanism is illustrated below in Figure 4.20, and the calculated PES for this mechanism in both benzene and methanol are shown in Figure 4.21.
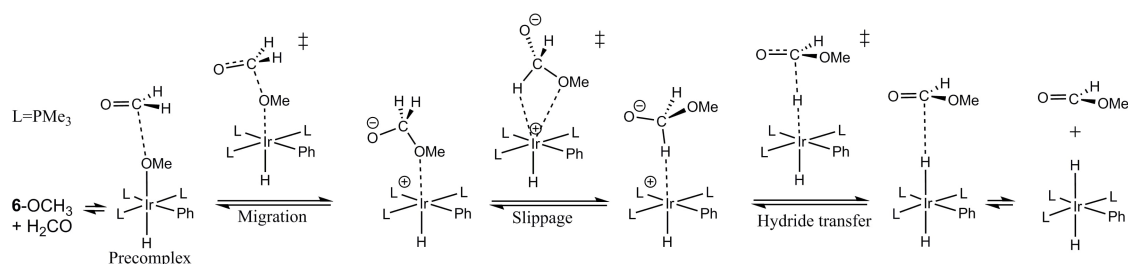
Figure 4.20: Illustration of the proposed dehydrogenative coupling mechanism facilitated by an H/OR metathesis mediated via an ion pair intermediate for the formation of methylformate from the reaction between **6-OCH₃** and formaldehyde.
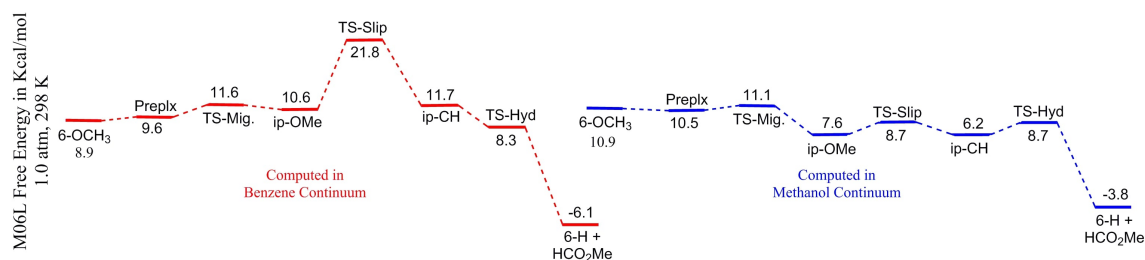
Figure 4.21: Energy profiles depicting the steps of methylformate formation from the reaction between **6-OCH₃** and formaldehyde in benzene and methanol continuum.

In the benzene continuum we observe that the rate determining step is the slippage transition state with a calculated free energy of 21.8 Kcal/mol. In Figure

4.18, we showed the catalytic effect of methanol on the system under study. The reaction for the formation of the methylformate also is catalysed by methanol, as is clearly evident from the lowered energy of the TS-Slip in Figure 4.21 to 8.7 Kcal/mol (lower by 13.1 Kcal/mol). Finally, the formation of the ester, unlike the aldehyde is shown to be a favored process over the complete PES (notice the PES in Figure 4.21 begins with the energies for the formation of the aldehyde in Figure 4.18.)

The methylformate product from the previous reaction can be perceived to undergo another H/OMe metathesis step resulting in the formation of a dimethylcarbonate molecule and a transhydride complex (Figure 4.22). The reaction energies in both benzene and methanol are calculated to be exergonic. The thermodynamic data calculated for the reaction between methylformate and **6-OCH₃**.
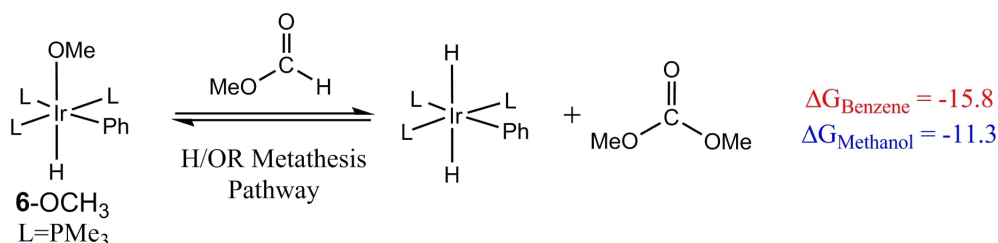
Figure 4.22: Reaction between **6-OCH₃** and methylformate computed in both benzene (red) and methanol (blue) relative to methylformate formation.

The reaction in Figure 4.14 was utilized as a case study for systems that lack cis-vacant site and yet can undergo dehydrogenative coupling of alcohols into aldehydes. While the original work concludes by the formation of aldehyde oligomers, we have reason to believe based on our detailed mechanistic investigation that the actual products of such a reaction will be the result coupling between the formed aldehyde and the metal alkoxides in the reaction mixtures giving the thermodynamically favorable ester products.

4.6 Conclusion

The octahedral complex **6-OCH₃** is a rare example that demonstrates without ambiguity that aldehyde deinsertion can take place from a metal-alkoxide by an unconventional outer-sphere mechanism that does not require an empty coordination site cis to the alkoxide. The reaction, however, requires an external alcohol as a catalyst. We became interested to know if the DFT methods that we routinely use to investigate reaction mechanism can reproduce the experimental observations available on this system. We show that accounting for solvent effect either

explicitly, by including one or two actual molecules of methanol, or implicitly, by applying solvent continuum methodologies, can both reproduce the observed catalytic effect of methanol. However, we compute formaldehyde deinsertion to be uphill. If this is true, the concentration of formaldehyde will be too low to drive formaldehyde oligomerization. Our calculations provide evidence that a formaldehyde molecule produced by deinsertion from a molecule of **6-OCH₃** can readily react with another **6-OCH₃** molecule by another outer-sphere mode to produce an ester and a trans-dihydride product. The latter step is highly exergonic. Consideration of this possibility leads to the conclusion that reaction of the square planar **6-Ir** and methanol affects at least in part the following stoichiometric alcohol dehydrogenative coupling reaction (Figure 4.23).
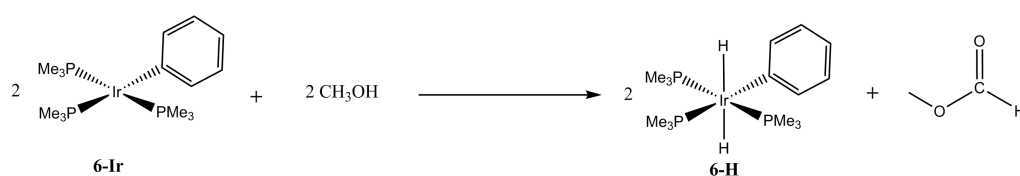
Figure 4.23: Stoichiometric alcohol dehydrogenative coupling reaction between **6-Ir** and methanol computed to give equivalents of **6-H** and methylformate.

Appendix A

Abbreviations

BDE	Bond Dissociation Energy
BINAP	2,2-bis(diphenylphosphino)-1,1-binaphthyl
DFT	Density Functional Theory
HAT	Hydrogen Atom Transfer
i	Intermediate
IRC	Intrinsic Reaction Coordinate
MLC	Metal-Ligand Cooperative
NAO	Natural Atomic Orbital
NBO	Natural Bonding Orbital
PCET	Proton Coupled Electron Transfer
PES	Potential Energy Surface
QTAIM	Quantum Theory of Atoms in Molecules
THF	Tetrahydrofuran
TS	Transition State
WFX	Wafefunction file

Appendix B

Run Script Samples

B.1   Optimization and Frequency

```
%chk=Sample
%mem=40GB
%NProcShared=28
#M06L/gen opt freq scrf=(smd,solvent=toluene) integral=(grid=superfine)

Sample

0 1
  C             0.59963855      1.27028666      0.00000000
  H             1.13280229      0.35290407     -0.13800581
  C            -0.94036145      1.27028666      0.00000000
  H            -1.29702780      0.26148088     -0.00000013
  H            -1.29702780      1.77468967      0.87365137
  H            -1.29702831      1.77468947     -0.87365128
  O             1.22667898      2.34919718      0.16230515

H C O 0
Def2TZVP
****
```

Figure B.1: An input file showing the text based commands required to run a geometry optimization job along with calculating the frequencies of the resultant minimum energy geometry.

```
                         ----------------------------
                         !   Optimized Parameters    !
                         ! (Angstroms and Degrees)   !
 --------------------------                              --------------------------
 ! Name  Definition           Value          Derivative Info.                  !
 --------------------------------------------------------------------------------
 ! R1     R(1,2)               1.1154         -DE/DX =    0.0                    !
 ! R2     R(1,3)               1.4867         -DE/DX =    0.0                    !
 ! R3     R(1,7)               1.2033         -DE/DX =    0.0                    !
 ! R4     R(3,4)               1.0917         -DE/DX =    0.0                    !
 ! R5     R(3,5)               1.0868         -DE/DX =    0.0                    !
 ! R6     R(3,6)               1.0917         -DE/DX =    0.0                    !
 ! A1     A(2,1,3)           114.4416         -DE/DX =    0.0                    !
 ! A2     A(2,1,7)           120.3039         -DE/DX =    0.0                    !
 ! A3     A(3,1,7)           125.2545         -DE/DX =    0.0                    !
 ! A4     A(1,3,4)           109.5471         -DE/DX =    0.0                    !
 ! A5     A(1,3,5)           111.8777         -DE/DX =    0.0                    !
 ! A6     A(1,3,6)           109.549          -DE/DX =    0.0                    !
 ! A7     A(4,3,5)           109.8737         -DE/DX =    0.0                    !
 ! A8     A(4,3,6)           105.9556         -DE/DX =    0.0                    !
 ! A9     A(5,3,6)           109.8638         -DE/DX =    0.0                    !
 ! D1     D(2,1,3,4)          57.8865         -DE/DX =    0.0                    !
 ! D2     D(2,1,3,5)        -180.0201         -DE/DX =    0.0                    !
 ! D3     D(2,1,3,6)         -57.938          -DE/DX =    0.0                    !
 ! D4     D(7,1,3,4)        -122.1225         -DE/DX =    0.0                    !
 ! D5     D(7,1,3,5)          -0.0291         -DE/DX =    0.0                    !
 ! D6     D(7,1,3,6)         122.053          -DE/DX =    0.0                    !
 --------------------------------------------------------------------------------
 GradGradGradGradGradGradGradGradGradGradGradGradGradGradGradGradGradGrad

                              Input orientation:
 ---------------------------------------------------------------------
 Center     Atomic     Atomic              Coordinates (Angstroms)
 Number     Number     Type          X           Y           Z
 ---------------------------------------------------------------------
    1          6          0        0.578350    1.332859    0.008709
    2          1          0        1.059880    0.569466   -0.646671
    3          6          0       -0.907566    1.285998    0.018473
    4          1          0       -1.239707    0.296122    0.337294
    5          1          0       -1.332425    2.045634    0.669299
    6          1          0       -1.283832    1.415806   -0.998103
    7          8          0        1.252975    2.107650    0.635298
 ---------------------------------------------------------------------
                       Distance matrix (angstroms):
                       1          2          3          4          5
     1  C     0.000000
     2  H     1.115421   0.000000
     3  C     1.486686   2.196970   0.000000
     4  H     2.118519   2.516149   1.091705   0.000000
     5  H     2.143709   3.103864   1.086796   1.783148   0.000000
     6  H     2.118554   2.516502   1.091721   1.743252   1.783052
     7  O     1.203343   2.011652   2.392388   3.095788   2.586367
                       6          7
     6  H     0.000000
     7  O     3.095487   0.000000
 Stoichiometry    C2H4O
 Framework group  C1[X(C2H4O)]
 Deg. of freedom    15
 Full point group                 C1      NOp   1
 Largest Abelian subgroup         C1      NOp   1
 Largest concise Abelian subgroup C1      NOp   1
                           Standard orientation:
 ---------------------------------------------------------------------
 Center     Atomic     Atomic              Coordinates (Angstroms)
 Number     Number     Type          X           Y           Z
 ---------------------------------------------------------------------
    1          6          0        0.227431    0.391153   -0.000026
    2          1          0        0.288238    1.504915    0.000090
    3          6          0       -1.157545   -0.149288   -0.000015
    4          1          0       -1.696673    0.227511   -0.871327
    5          1          0       -1.168189   -1.236032   -0.000486
    6          1          0       -1.696338    0.226580    0.871925
    7          8          0        1.231705   -0.271771    0.000006
 ---------------------------------------------------------------------
 Rotational constants (GHZ):     58.0584614   10.2352791    9.1856809
```

Figure B.2: An output file showing the optimized geometric parameters for the submitted geometry in figure B.1.

69

```
Harmonic frequencies (cm**-1), IR intensities (KM/Mole), Raman scattering
activities (A**4/AMU), depolarization ratios for plane and unpolarized
incident light, reduced masses (AMU), force constants (mDyne/A),
and normal coordinates:
                          1                         2                         3
                          A                         A                         A
Frequencies --      182.1215                  512.0619                  781.5488
Red. masses --        1.2394                    2.5100                    1.1174
Frc consts  --        0.0242                    0.3878                    0.4021
IR Inten    --        0.3823                   15.7165                    0.8397
 Atom  AN      X      Y      Z        X      Y      Z        X      Y      Z
   1   6     0.00   0.00   0.11     0.02   0.21   0.00     0.00   0.00  -0.06
   2   1     0.00   0.00   0.31     0.23   0.19   0.00     0.00   0.00   0.60
   3   6     0.00   0.00   0.00     0.16  -0.02   0.00     0.00   0.00  -0.08
   4   1     0.29  -0.38  -0.35    -0.02  -0.34  -0.02    -0.46  -0.21   0.13
   5   1     0.00   0.00   0.41     0.75  -0.03   0.00     0.00   0.00   0.29
   6   1    -0.29   0.38  -0.35    -0.02  -0.34   0.02     0.46   0.21   0.13
   7   8     0.00   0.00  -0.08    -0.19  -0.11   0.00     0.00   0.00   0.03
                          4                         5                         6
                          A                         A                         A
Frequencies --      905.8471                 1140.7028                 1142.8779
Red. masses --        2.0724                    2.1225                    1.8102
Frc consts  --        1.0019                    1.6272                    1.3931
IR Inten    --       10.8259                   33.3897                    1.2586
 Atom  AN      X      Y      Z        X      Y      Z        X      Y      Z
   1   6    -0.12  -0.07   0.00     0.14   0.20   0.00     0.00   0.00   0.22
   2   1    -0.39  -0.05   0.00     0.11   0.21   0.00     0.00   0.00  -0.72
   3   6     0.24  -0.03   0.00    -0.03  -0.19   0.00     0.00   0.00  -0.14
   4   1     0.44   0.39   0.05     0.02   0.22   0.13    -0.38  -0.04   0.10
   5   1    -0.23  -0.01   0.00    -0.82  -0.18   0.00     0.00   0.00   0.32
   6   1     0.44   0.39  -0.05     0.02   0.22  -0.13     0.38   0.04   0.10
   7   8    -0.11   0.03   0.00    -0.04  -0.03   0.00     0.00   0.00  -0.05
                          7                         8                         9
                          A                         A                         A
Frequencies --     1379.8569                 1425.2760                 1456.6273
Red. masses --        1.2576                    1.1938                    1.0812
Frc consts  --        1.4108                    1.4289                    1.3516
IR Inten    --       33.5157                   15.9353                   28.5380
 Atom  AN      X      Y      Z        X      Y      Z        X      Y      Z
   1   6    -0.01  -0.01   0.00    -0.06  -0.06   0.00     0.00   0.02   0.00
   2   1    -0.26   0.00   0.00     0.92  -0.14   0.00    -0.20   0.03   0.00
   3   6     0.14   0.06   0.00     0.04  -0.03   0.00    -0.03  -0.05   0.00
   4   1    -0.52  -0.19   0.29    -0.13   0.12   0.17    -0.20   0.44   0.31
   5   1    -0.36   0.06   0.00    -0.03  -0.03   0.00     0.53  -0.05   0.00
   6   1    -0.52  -0.19  -0.29    -0.13   0.12  -0.17    -0.21   0.44  -0.31
   7   8     0.01  -0.01   0.00    -0.03   0.07   0.00     0.03  -0.03   0.00
                         10                        11                        12
                          A                         A                         A
Frequencies --     1467.2795                 1827.8291                 2845.2997
Red. masses --        1.0460                    9.2403                    1.0820
Frc consts  --        1.3268                   18.1890                    5.1612
IR Inten    --       11.5589                  252.4112                  155.7416
 Atom  AN      X      Y      Z        X      Y      Z        X      Y      Z
   1   6     0.00   0.00  -0.03     0.60  -0.33   0.00    -0.01  -0.08   0.00
   2   1     0.00   0.00   0.09    -0.38  -0.20   0.00     0.08   0.99   0.00
   3   6     0.00   0.00  -0.05    -0.05   0.02   0.00     0.00   0.00   0.00
   4   1     0.17   0.45   0.05    -0.17   0.04   0.10     0.01  -0.01   0.02
   5   1     0.00   0.00   0.72     0.26  -0.01   0.00     0.00  -0.01   0.00
   6   1    -0.17  -0.45   0.05    -0.17   0.04  -0.10     0.01  -0.01  -0.02
   7   8     0.00   0.00   0.00    -0.38   0.25   0.00     0.00   0.00   0.00
                         13                        14                        15
                          A                         A                         A
Frequencies --     3057.9823                 3137.7887                 3186.2438
Red. masses --        1.0372                    1.0983                    1.1048
Frc consts  --        5.7148                    6.3711                    6.6086
IR Inten    --        0.4247                    2.2220                   11.0219
 Atom  AN      X      Y      Z        X      Y      Z        X      Y      Z
   1   6     0.00   0.00   0.00     0.00   0.00   0.00     0.00   0.00   0.00
   2   1    -0.01  -0.02   0.00     0.00   0.00   0.00     0.00  -0.02   0.00
   3   6    -0.05   0.00   0.00     0.00   0.00   0.09    -0.02   0.09   0.00
   4   1     0.30  -0.21   0.50    -0.36   0.25  -0.55     0.16  -0.10   0.27
   5   1     0.00   0.47   0.00     0.00   0.00   0.01    -0.01  -0.88   0.00
   6   1     0.30  -0.21  -0.50     0.36  -0.25  -0.55     0.16  -0.10  -0.27
   7   8     0.00   0.00   0.00     0.00   0.00   0.00     0.00   0.00   0.00
```

Figure B.3: An output file showing the calculated frequencies and other information based on the optimized geometry.

```
--------------------
- Thermochemistry -
--------------------
Temperature   298.150 Kelvin.  Pressure   1.00000 Atm.
Atom     1 has atomic number  6 and mass  12.00000
Atom     2 has atomic number  1 and mass   1.00783
Atom     3 has atomic number  6 and mass  12.00000
Atom     4 has atomic number  1 and mass   1.00783
Atom     5 has atomic number  1 and mass   1.00783
Atom     6 has atomic number  1 and mass   1.00783
Atom     7 has atomic number  8 and mass  15.99491
Molecular mass:    44.02621 amu.
Principal axes and moments of inertia in atomic units:
                        1         2         3
    Eigenvalues --   31.08490 176.32555 196.47332
          X           0.99968   0.02529   0.00000
          Y          -0.02529   0.99968   0.00001
          Z           0.00000  -0.00001   1.00000
This molecule is an asymmetric top.
Rotational symmetry number  1.
Rotational temperatures (Kelvin)      2.78636     0.49122     0.44084
Rotational constants (GHZ):          58.05846    10.23528     9.18568
Zero-point vibrational energy      146239.5 (Joules/Mol)
                                       34.95209 (Kcal/Mol)
Warning -- explicit consideration of   2 degrees of freedom as
          vibrations may cause significant error
Vibrational temperatures:     262.03    736.74   1124.47   1303.31   1641.21
         (Kelvin)            1644.34   1985.30   2050.65   2095.76   2111.09
                            2629.84   4093.75   4399.75   4514.57   4584.29

Zero-point correction=                           0.055700 (Hartree/Particle)
Thermal correction to Energy=                    0.059543
Thermal correction to Enthalpy=                  0.060488
Thermal correction to Gibbs Free Energy=         0.030867
Sum of electronic and zero-point Energies=            -153.819813
Sum of electronic and thermal Energies=               -153.815969
Sum of electronic and thermal Enthalpies=             -153.815025
Sum of electronic and thermal Free Energies=          -153.844645

                    E (Thermal)             CV                S
                     KCal/Mol          Cal/Mol-Kelvin    Cal/Mol-Kelvin
Total                  37.364              11.120            62.342
Electronic              0.000               0.000             0.000
Translational           0.889               2.981            37.273
Rotational              0.889               2.981            21.604
Vibrational            35.587               5.158             3.466
Vibration     1         0.630               1.864             2.307
Vibration     2         0.867               1.223             0.629
                    Q                 Log10(Q)            Ln(Q)
Total Bot        0.634271D-14        -14.197725         -32.691470
Total V=0        0.264426D+12         11.422305          26.300829
Vib (Bot)        0.470243D-25        -25.327678         -58.319134
Vib (Bot)     1  0.110203D+01          0.042193           0.097152
Vib (Bot)     2  0.317512D+00         -0.498240          -1.147241
Vib (V=0)        0.196043D+01          0.292352           0.673165
Vib (V=0)     1  0.171015D+01          0.233034           0.536582
Vib (V=0)     2  0.109230D+01          0.038340           0.088281
Electronic       0.100000D+01          0.000000           0.000000
Translational    0.114821D+08          7.060022          16.256302
Rotational       0.117471D+05          4.069931           9.371361
***** Axes restored to original set *****
-------------------------------------------------------------------
Center     Atomic                   Forces (Hartrees/Bohr)
Number     Number            X              Y              Z
-------------------------------------------------------------------
   1          6         -0.000053309    0.000015885   -0.000014415
   2          1          0.000051897    0.000051615    0.000048035
   3          6         -0.000001084   -0.000041113   -0.000034214
   4          1          0.000026158   -0.000035480   -0.000003470
   5          1         -0.000031274   -0.000020546   -0.000010397
   6          1          0.000039522   -0.000015804   -0.000034048
   7          8         -0.000031910    0.000045442    0.000048510
-------------------------------------------------------------------
Cartesian Forces:  Max    0.000053309 RMS    0.000034983
FormGI is forming the generalized inverse of G from B-inverse, IUseBI=4.
```

Figure B.4: An output file showing the thermochemistry section from the frequency calculation job. The thermodynamic data summarized in this figure, are used to calculate the PES.

B.2 Natural Bonding Orbitals (NBO) Analysis

```
%chk=Sample
%mem=40GB
%NProcShared=28
#M06L/gen scrf=(smd,solvent=toluene) integral=(grid=superfine) pop=(NBOread)

Sample

0 1
 C                 0.59963855     1.27028666      0.00000000
 H                 1.13280229     0.35290407     -0.13800581
 C                -0.94036145     1.27028666      0.00000000
 H                -1.29702780     0.26148088     -0.00000013
 H                -1.29702780     1.77468967      0.87365137
 H                -1.29702831     1.77468947     -0.87365128
 O                 1.22667898     2.34919718      0.16230515

H C O O
Def2TZVP
****

$NBO PLOT $END
```

Figure B.5: An input file showing the text based commands required to print out the NBOs of an optimized geometry.

```
NATURAL POPULATIONS:  Natural atomic orbital occupancies

 NAO  Atom  No  lang   Type(AO)    Occupancy      Energy
--------------------------------------------------------------
   1    C    1   s    Cor( 1S)     1.99962      -10.02723
   2    C    1   s    val( 2S)     1.00631       -0.28219
   3    C    1   s    Ryd( 4S)     0.00699        1.11902
   4    C    1   s    Ryd( 3S)     0.00010        0.77975
   5    C    1   s    Ryd( 5S)     0.00000       21.77754
   6    C    1   px   val( 2p)     0.85073       -0.04032
   7    C    1   px   Ryd( 4p)     0.00667        1.04919
   8    C    1   px   Ryd( 3p)     0.00019        0.96798
   9    C    1   py   val( 2p)     0.99923       -0.05156
  10    C    1   py   Ryd( 4p)     0.00259        1.19369
  11    C    1   py   Ryd( 3p)     0.00020        0.96938
  12    C    1   pz   val( 2p)     0.68260       -0.13903
  13    C    1   pz   Ryd( 4p)     0.00066        0.86813
  14    C    1   pz   Ryd( 3p)     0.00037        0.83212
  15    C    1   dxy  Ryd( 4d)     0.00064        3.60779
  16    C    1   dxy  Ryd( 3d)     0.00020        2.43759
  17    C    1   dxz  Ryd( 4d)     0.00082        3.02658
  18    C    1   dxz  Ryd( 3d)     0.00011        1.89183
  19    C    1   dyz  Ryd( 4d)     0.00023        2.84016
  20    C    1   dyz  Ryd( 3d)     0.00004        1.73706
  21    C    1   dx2y2 Ryd( 4d)    0.00172        3.45064
  22    C    1   dx2y2 Ryd( 3d)    0.00005        2.51520
  23    C    1   dz2  Ryd( 4d)     0.00022        3.21007
  24    C    1   dz2  Ryd( 3d)     0.00016        1.95727
  25    C    1   f(0)  Ryd( 4f)    0.00012        3.26630
  26    C    1   f(C1) Ryd( 4f)    0.00010        3.37090
  27    C    1   f(S1) Ryd( 4f)    0.00003        3.32863
  28    C    1   f(C2) Ryd( 4f)    0.00001        3.27678
  29    C    1   f(S2) Ryd( 4f)    0.00002        3.33279
  30    C    1   f(C3) Ryd( 4f)    0.00005        3.90820
  31    C    1   f(S3) Ryd( 4f)    0.00021        3.97121

  32    H    2   s    val( 1S)     0.89199       -0.05138
  33    H    2   s    Ryd( 2S)     0.00234        0.49265
  34    H    2   s    Ryd( 3S)     0.00016        2.05409
  35    H    2   px   Ryd( 2p)     0.00038        2.26207
  36    H    2   py   Ryd( 2p)     0.00061        3.03472
  37    H    2   pz   Ryd( 2p)     0.00013        1.98085

  38    C    3   s    Cor( 1S)     1.99943       -9.90415
  39    C    3   s    val( 2S)     1.15233       -0.32189
  40    C    3   s    Ryd( 3S)     0.00092        0.87846
  41    C    3   s    Ryd( 4S)     0.00011        2.29118
  42    C    3   s    Ryd( 5S)     0.00000       21.29181
  43    C    3   px   val( 2p)     1.10372       -0.10855
  44    C    3   px   Ryd( 3p)     0.00120        0.64787
  45    C    3   px   Ryd( 4p)     0.00024        1.41527
  46    C    3   py   val( 2p)     1.19963       -0.10388
  47    C    3   py   Ryd( 3p)     0.00073        0.71052
  48    C    3   py   Ryd( 4p)     0.00006        1.40382
  49    C    3   pz   val( 2p)     1.22128       -0.10869
  50    C    3   pz   Ryd( 3p)     0.00029        0.68410
  51    C    3   pz   Ryd( 4p)     0.00003        1.39298
  52    C    3   dxy  Ryd( 4d)     0.00070        3.05342
  53    C    3   dxy  Ryd( 3d)     0.00013        2.13496
  54    C    3   dxz  Ryd( 4d)     0.00015        2.62860
  55    C    3   dxz  Ryd( 3d)     0.00006        1.83744
  56    C    3   dyz  Ryd( 4d)     0.00029        2.99285
  57    C    3   dyz  Ryd( 3d)     0.00017        2.04499
  58    C    3   dx2y2 Ryd( 4d)    0.00045        2.85473
  59    C    3   dx2y2 Ryd( 3d)    0.00010        2.22076
  60    C    3   dz2  Ryd( 4d)     0.00033        2.94399
  61    C    3   dz2  Ryd( 3d)     0.00010        2.21864
  62    C    3   f(0)  Ryd( 4f)    0.00003        3.28583
  63    C    3   f(C1) Ryd( 4f)    0.00005        3.35404
  64    C    3   f(S1) Ryd( 4f)    0.00022        3.69167
  65    C    3   f(C2) Ryd( 4f)    0.00003        3.35446
  66    C    3   f(S2) Ryd( 4f)    0.00003        3.30425
  67    C    3   f(C3) Ryd( 4f)    0.00007        3.47017
  68    C    3   f(S3) Ryd( 4f)    0.00021        3.48787

  69    H    4   s    val( 1S)     0.79571       -0.00150
  70    H    4   s    Ryd( 2S)     0.00044        0.80514
  71    H    4   s    Ryd( 3S)     0.00010        1.52544
  72    H    4   px   Ryd( 2p)     0.00031        2.56453
  73    H    4   py   Ryd( 2p)     0.00033        2.53912
  74    H    4   pz   Ryd( 2p)     0.00014        2.08632
```

Figure B.6: An output file showing the first section from the NBO analysis. This section includes the designation of the natural atomic orbitals (NAO) and given in a numbered order which is important for conducting further analysis.

```
NATURAL BOND ORBITAL ANALYSIS:

                     Occupancies     Lewis Structure    Low   High
             Occ.   ------------     ----------------   occ   occ
Cycle  Thresh.   Lewis   Non-Lewis   CR  BD  3C  LP    (L)   (NL)   Dev
=======================================================================
1(1)    1.90   23.31480   0.68520     3   8   0   1     3     2    0.06
2(2)    1.90   23.31480   0.68520     3   8   0   1     3     2    0.06
3(1)    1.80   23.79811   0.20189     3   7   0   2     0     0    0.06
-----------------------------------------------------------------------

Structure accepted: No low occupancy Lewis orbitals

---------------------------------------------------------------
 Core                    5.99886 ( 99.981% of     6)
 Valence Lewis          17.79924 ( 98.885% of    18)
==================     ==============================
 Total Lewis            23.79811 ( 99.159% of    24)
---------------------------------------------------------------
 Valence non-Lewis       0.17596 (  0.733% of    24)
 Rydberg non-Lewis       0.02593 (  0.108% of    24)
==================     ==============================
 Total non-Lewis         0.20189 (  0.841% of    24)
---------------------------------------------------------------


       (Occupancy)  Bond orbital/ Coefficients/ Hybrids
-------------------------------------------------------------------------
  1. (1.99136) BD ( 1) C   1 - H   2
             ( 56.93%)  0.7545* C   1 s( 32.34%)p 2.09( 67.61%)d 0.00(  0.05%)
                                           f 0.00(  0.00%)
                            -0.0001   0.5674  -0.0373  -0.0018  -0.0005
                             0.1160  -0.0020  -0.0016   0.8138  -0.0138
                            -0.0117   0.0016   0.0001  -0.0001   0.0043
                            -0.0028   0.0000   0.0001   0.0001   0.0002
                            -0.0207   0.0006  -0.0081   0.0003   0.0000
                             0.0006  -0.0029   0.0000  -0.0001   0.0009
                            -0.0031
             ( 43.07%)  0.6563* H   2 s( 99.93%)p 0.00(  0.07%)
                             0.9996  -0.0103   0.0001  -0.0040  -0.0252
                             0.0000
  2. (1.99596) BD ( 1) C   1 - C   3
             ( 48.08%)  0.6934* C   1 s( 35.25%)p 1.84( 64.68%)d 0.00(  0.06%)
                                           f 0.00(  0.02%)
                             0.0000   0.5937  -0.0028   0.0056   0.0003
                            -0.7429  -0.0045   0.0067  -0.3078   0.0104
                             0.0005  -0.0012  -0.0004   0.0001   0.0155
                             0.0005   0.0000  -0.0003  -0.0001  -0.0003
                             0.0138   0.0019  -0.0099   0.0044  -0.0001
                             0.0066   0.0004   0.0002   0.0001  -0.0030
                            -0.0108
             ( 51.92%)  0.7206* C   3 s( 25.15%)p 2.97( 74.77%)d 0.00(  0.07%)
                                           f 0.00(  0.02%)
                             0.0000   0.5012  -0.0180  -0.0054   0.0004
                             0.7882   0.0081  -0.0118   0.3552   0.0015
                            -0.0034  -0.0021   0.0012  -0.0003   0.0162
                             0.0038   0.0003   0.0006   0.0000   0.0000
                             0.0154   0.0039  -0.0110   0.0016   0.0037
                             0.0016  -0.0096   0.0019   0.0021   0.0053
                             0.0060
  3. (1.99798) BD ( 1) C   1 - O   7
             ( 35.72%)  0.5976* C   1 s( 32.78%)p 2.05( 67.14%)d 0.00(  0.06%)
                                           f 0.00(  0.01%)
                             0.0000   0.5692   0.0621  -0.0055   0.0006
                             0.6560   0.0537   0.0001  -0.4875  -0.0221
                             0.0047  -0.0015   0.0000   0.0000  -0.0138
                             0.0153  -0.0001  -0.0002  -0.0001  -0.0002
                             0.0042  -0.0036  -0.0062   0.0105   0.0000
                            -0.0042   0.0017   0.0000   0.0000  -0.0054
                            -0.0081
             ( 64.28%)  0.8018* O   7 s( 34.15%)p 1.91( 65.30%)d 0.02(  0.54%)
                                           f 0.00(  0.01%)
                             0.0000   0.5841  -0.0204   0.0009   0.0004
                            -0.6350   0.0141   0.0092   0.4993  -0.0115
                            -0.0054  -0.0013   0.0001   0.0000  -0.0624
                             0.0002   0.0000   0.0000  -0.0001   0.0000
                             0.0168  -0.0001  -0.0347  -0.0001   0.0000
                             0.0038  -0.0029   0.0000   0.0000   0.0031
                             0.0080
```

Figure B.7: An output file showing the NBO analysis section for the optimized geometry. In this section the bonding (BD) lone pairs (LP) and other types of orbitals are shown along with informaton regarding the NAOs that compromise them.

B.3 Quantum Theory of Atoms in Molecules (QTAIM) Analysis

```
%chk=Sample
%mem=40GB
%NProcShared=28
#M06L/gen scrf=(smd,solvent=toluene) integral=(grid=superfine) Density=current output=wfx


Sample

0 1
 C                 0.59963855      1.27028666      0.00000000
 H                 1.13280229      0.35290407     -0.13800581
 C                -0.94036145      1.27028666      0.00000000
 H                -1.29702780      0.26148088     -0.00000013
 H                -1.29702780      1.77468967      0.87365137
 H                -1.29702831      1.77468947     -0.87365128
 O                 1.22667898      2.34919718      0.16230515

H C O O
Def2TZVP
****

Sample.wfx
```

Figure B.8: An input file showing the text based commands required to generate an wavefunction file (WFX) in order to conduct QTAIM analysis on another software AIMALL.

Bibliography

[1] R. H. Dalitz and R. E. Peierls, "Paul adrien maurice dirac, 8 august 1902-20 october 1984," 1986.

[2] H. Tanaka, Y. Nishibayashi, and K. Yoshizawa, "Interplay between theory and experiment for ammonia synthesis catalyzed by transition metal complexes," *Accounts of chemical research*, vol. 49, no. 5, pp. 987–995, 2016.

[3] Y. Park, S. Ahn, D. Kang, and M.-H. Baik, "Mechanism of rh-catalyzed oxidative cyclizations: closed versus open shell pathways," *Accounts of chemical research*, vol. 49, no. 6, pp. 1263–1270, 2016.

[4] X. Zhang, L. W. Chung, and Y.-D. Wu, "New mechanistic insights on the selectivity of transition-metal-catalyzed organic reactions: The role of computational chemistry," *Accounts of chemical research*, vol. 49, no. 6, pp. 1302–1310, 2016.

[5] P. Richardson, I. Griffin, C. Tucker, D. Smith, O. Oechsle, A. Phelan, and J. Stebbing, "Baricitinib as potential treatment for 2019-ncov acute respiratory disease," *Lancet (London, England)*, vol. 395, no. 10223, p. e30, 2020.

[6] M. J. Frisch, G. W. Trucks, H. B. Schlegel, G. E. Scuseria, M. A. Robb, J. R. Cheeseman, G. Scalmani, V. Barone, B. Mennucci, G. A. Petersson, H. Nakatsuji, M. Caricato, X. Li, H. P. Hratchian, A. F. Izmaylov, J. Bloino, G. Zheng, J. L. Sonnenberg, M. Hada, M. Ehara, K. Toyota, R. Fukuda, J. Hasegawa, M. Ishida, T. Nakajima, Y. Honda, O. Kitao, H. Nakai, T. Vreven, J. A. Montgomery, Jr., J. E. Peralta, F. Ogliaro, M. Bearpark, J. J. Heyd, E. Brothers, K. N. Kudin, V. N. Staroverov, R. Kobayashi, J. Normand, K. Raghavachari, A. Rendell, J. C. Burant, S. S. Iyengar, J. Tomasi, M. Cossi, N. Rega, J. M. Millam, M. Klene, J. E. Knox, J. B. Cross, V. Bakken, C. Adamo, J. Jaramillo, R. Gomperts, R. E. Stratmann, O. Yazyev, A. J. Austin, R. Cammi, C. Pomelli, J. W. Ochterski, R. L. Martin, K. Morokuma, V. G. Zakrzewski, G. A. Voth, P. Salvador, J. J. Dannenberg, S. Dapprich, A. D. Daniels, O. Farkas, J. B. Foresman, J. V. Ortiz, J. Cioslowski, and D. J. Fox, "Gaussian 09 Revision E.01."

[7] Y. Zhao and D. G. Truhlar, "The m06 suite of density functionals for main group thermochemistry, thermochemical kinetics, noncovalent interactions, excited states, and transition elements: two new functionals and systematic testing of four m06-class functionals and 12 other functionals," *Theoretical Chemistry Accounts*, vol. 120, no. 1-3, pp. 215–241, 2008.

[8] Y. Zhao and D. G. Truhlar, "A new local density functional for main-group thermochemistry, transition metal bonding, thermochemical kinetics, and noncovalent interactions," *The Journal of chemical physics*, vol. 125, no. 19, p. 194101, 2006.

[9] J.-D. Chai and M. Head-Gordon, "Long-range corrected hybrid density functionals with damped atom–atom dispersion corrections," *Physical Chemistry Chemical Physics*, vol. 10, no. 44, pp. 6615–6620, 2008.

[10] D. Andrae, U. Haeussermann, M. Dolg, H. Stoll, and H. Preuss, "Energy-adjustedab initio pseudopotentials for the second and third row transition elements," *Theoretica chimica acta*, vol. 77, no. 2, pp. 123–141, 1990.

[11] J. E. C. E. D. Glendening, A. E. Reed and F. Weinhold, "Nbo version 3.1."

[12] Z. G. A, "Chemcraft - graphical program for visualization of quantum chemistry computations. ivanovo, russia, 2005."

[13] R. Dennington, T. A. Keith, and J. M. Millam, "Gaussview Version 5," 2000. Semichem Inc. Shawnee Mission KS.

[14] T. G. S. Todd A. Keith, "Aimall (version 19.10.12)."

[15] V. Pattabathula and J. Richardson, "Introduction to ammonia production." https://www.aiche.org/resources/publications/cep/2016/september/introduction-ammonia-production, September 2016.

[16] P. Morrison, "From fertile minds." https://web.archive.org/web/20120702093415/http://www.americanscientist.org/bookshelf/pub/from-fertile-minds, 2001.

[17] M. Jewess and R. H. Crabtree, "Electrocatalytic nitrogen fixation for distributed fertilizer production?," 2016.

[18] the-compost gardener.com, "The haber process nitrogen fertilizer from the air." https://www.the-compost-gardener.com/haber-process.html, January 2020.

[19] C. E. Laplaza and C. C. Cummins, "Dinitrogen cleavage by a three-coordinate molybdenum (iii) complex," *Science*, vol. 268, no. 5212, pp. 861–863, 1995.

[20] A. Logadottir and J. K. Nørskov, "Ammonia synthesis over a ru (0001) surface studied by density functional calculations," *Journal of Catalysis*, vol. 220, no. 2, pp. 273–279, 2003.

[21] T. J. Hebden, R. R. Schrock, M. K. Takase, and P. Müller, "Cleavage of dinitrogen to yield a (t-bupocop) molybdenum (iv) nitride," *Chemical Communications*, vol. 48, no. 13, pp. 1851–1853, 2012.

[22] B. M. Lindley, Q. J. Bruch, P. S. White, F. Hasanayn, and A. J. Miller, "Ammonia synthesis from a pincer ruthenium nitride via metal–ligand cooperative proton-coupled electron transfer," *Journal of the American Chemical Society*, vol. 139, no. 15, pp. 5305–5308, 2017.

[23] F. Weinhold, C. Landis, and E. Glendening, "What is nbo analysis and how is it useful?," *International reviews in physical chemistry*, vol. 35, no. 3, pp. 399–440, 2016.

[24] F. W. Biegler-könig, R. F. Bader, and T.-H. Tang, "Calculation of the average properties of atoms in molecules. ii," *Journal of Computational Chemistry*, vol. 3, no. 3, pp. 317–328, 1982.

[25] L. P. Hammett, "The effect of structure upon the reactions of organic compounds. benzene derivatives," *Journal of the American Chemical Society*, vol. 59, no. 1, pp. 96–103, 1937.

[26] C. Hansch, A. Leo, and R. Taft, "A survey of hammett substituent constants and resonance and field parameters," *Chemical reviews*, vol. 91, no. 2, pp. 165–195, 1991.

[27] J. Barbosa, D. Barrón, E. Bosch, and M. Rosés, "Resolution of acid strength in tetrahydrofuran of substituted benzoic acids," *Analytica chimica acta*, vol. 265, no. 1, pp. 157–165, 1992.

[28] L. P. Hammett, "Some relations between reaction rates and equilibrium constants.," *Chemical Reviews*, vol. 17, no. 1, pp. 125–136, 1935.

[29] S.-I. Murahashi, K.-i. Ito, T. Naota, and Y. Maeda, "Ruthenium catalyzed transformation of alcohols to esters and lactones," *Tetrahedron Letters*, vol. 22, no. 52, pp. 5327–5330, 1981.

[30] K. Abdur-Rashid, S. E. Clapham, A. Hadzovic, J. N. Harvey, A. J. Lough, and R. H. Morris, "Mechanism of the hydrogenation of ketones catalyzed by trans-dihydrido (diamine) ruthenium (ii) complexes," *Journal of the American Chemical Society*, vol. 124, no. 50, pp. 15104–15118, 2002.

[31] R. J. Hamilton, C. G. Leong, G. Bigam, M. Miskolzie, and S. H. Bergens, "A ruthenium- dihydrogen putative intermediate in ketone hydrogenation," *Journal of the American Chemical Society*, vol. 127, no. 12, pp. 4152–4153, 2005.

[32] J. Zhang, G. Leitus, Y. Ben-David, and D. Milstein, "Efficient homogeneous catalytic hydrogenation of esters to alcohols," *Angewandte Chemie International Edition*, vol. 45, no. 7, pp. 1113–1115, 2006.

[33] F. Hasanayn and R. H. Morris, "Symmetry aspects of h2 splitting by five-coordinate d6 ruthenium amides, and calculations on acetophenone hydrogenation, ruthenium alkoxide formation, and subsequent hydrogenolysis in a model trans-ru (h) 2 (diamine)(diphosphine) system," *Inorganic chemistry*, vol. 51, no. 20, pp. 10808–10818, 2012.

[34] F. Hasanayn, L. M. Al-Assi, R. N. Moussawi, and B. S. Omar, "Mechanism of alcohol–water dehydrogenative coupling into carboxylic acid using milstein's catalyst: A detailed investigation of the outer-sphere pes in the reaction of aldehydes with an octahedral ruthenium hydroxide," *Inorganic chemistry*, vol. 55, no. 16, pp. 7886–7902, 2016.

[35] F. Hasanayn, A. Baroudi, A. A. Bengali, and A. S. Goldman, "Hydrogenation of dimethyl carbonate to methanol by trans-[ru (h) 2 (pnn)(co)] catalysts: Dft evidence for ion-pair-mediated metathesis paths for c–ome bond cleavage," *Organometallics*, vol. 32, no. 23, pp. 6969–6985, 2013.

[36] O. Blum and D. Milstein, "Hydride elimination from an iridium (iii) alkoxide complex: a case in which a vacant cis coordination site is not required," *Journal of Organometallic Chemistry*, vol. 593, pp. 479–484, 2000.